Stability of perpendicular magnetohydrodynamic shocks in materials with ideal and nonideal equations of state

A. Calvo-Rivera [*] and C. Huete
Grupo de Mecánica de Fluidos, Departamento de Ingeniería Térmica y de Fluidos,
Universidad Carlos III de Madrid, Leganés 28911, Spain

F. García-Rubio
Laboratory for Laser Energetics, University of Rochester, Rochester, New York 14627, USA
and Department of Mechanical Engineering, University of Rochester, Rochester, New York 14627, USA

A. L. Velikovich
Plasma Physics Division, U.S. Naval Research Laboratory, Washington, District of Columbia 20375, USA

R. Betti
Laboratory for Laser Energetics, University of Rochester, Rochester, New York 14627, USA;
Department of Mechanical Engineering, University of Rochester, Rochester, New York 14627, USA;
and Department of Physics and Astronomy, University of Rochester, Rochester, New York, New York 14627, USA

P. Tzeferacos
Department of Physics and Astronomy and Laboratory for Laser Energetics, University of Rochester, Rochester, New York 14627, USA
and Laboratory for Laser Energetics, University of Rochester, Rochester, New York 14627, USA

Magnetized target fusion approach to inertial confinement fusion involves the formation of strong shocks that travel along a magnetized plasma. Shocks, which play a dominant role in thermalizing the upstream kinetic energy generated in the implosion stage, are seldom free from perturbations, and they wrinkle in response to upstream or downstream disturbances. In Z-pinch experiments, significant plasma instability mitigation was observed with pre-embedded axial magnetic fields. To isolate effects, in this work we theoretically study the impact of perpendicular magnetic fields on the planar shock dynamics for different equations of state. For fast magnetosonic shocks in ideal gases, it was found that the magnetic field amplifies the intensity of the perturbations when $\gamma > 2$ or it weakens them when $\gamma < 2$. Weak shocks have been found to be stable regardless of the magnetic plasma intensity and gas compressibility; however, for sufficiently strong shocks the magnetic fields can promote a neutral stability/SAE at the shock if the adiabatic index is higher than $1 + \sqrt{2}$. Results have been validated with numerical simulations performed with the FLASH code.

I. INTRODUCTION

The recent remarkable breakthrough of the inertial confinement fusion (ICF) ignition on the National Ignition Facility (NIF) laser facility at Lawrence Livermore National Laboratory [1,2] puts to rest questions about the capability of lasers to ignite thermonuclear fuel [2]. This achievement sheds new light on the benefits of magnetizing ICF targets for achieving magnetoinertial fusion [3–9], a concept that stems from the well-established research field of magnetized target fusion, which first introduced the principle of inertial confinement of fusion plasma. More recent incarnations of the original Linhart's cylindrical-liner-on-magnetized plasma scheme [10] promise high fusion energy gains and multi-MJ yields in next-generation pulsed power facilities. This refers in particular to the magnetized liner inertial fusion (MagLIF) concept, which is now actively developed in the U.S.; see Refs. [11–15] and references therein. Among its alternatives, we note the staged Z-pinch (SZP) approach [16–22] that generated interest and some controversy [23–27]. Following Jones and Mead [28], the magnetization of ICF targets spherically imploded by x-rays or direct laser irradiation has also attracted considerable interest, particularly for the indirect drive [29]. It has already been demonstrated in the National Ignition Facility (NIF) experiments that target magnetization increases the ion temperature at stagnation and the fusion neutron yield [30]. Simulations for ignition-scale layered cryogenic targets predict that magnetization can make the NIF indirect-drive ignition more robust and increase the fusion energy gain [31,32].

In indirect- [1,2,33] and direct-drive [34] laser fusion, the propagation of shock waves in the early stages of

---
[*]andcalvo@ing.uc3m.es

implosion plays an essential role in determining its outcome. Similarly, for magnetically assisted indirect-drive laser fusion [28–32], the shock waves conventionally set the shell to the desired adiabat and preheat the hot spot while seeding some of the target perturbations/nonuniformities to be later amplified by the Rayleigh-Taylor instability [35–37]. In MagLIF [11–15], a blast wave launched by the laser preheat of the cold gaseous fuel determines the initial temperature and density profiles, as well as the uniformity of the DT plasma compressed by the liner. It has been observed that the unstable flute modes related to the magnetic Rayleigh-Taylor instability diminished, but a different helical-type instability may rise due to the effect of the magnetic field [38]. In SZP [16–27] converging shocks play an even more significant role in shaping the converging plasma and ensuring compression stability. In all these examples, the early shock waves propagate through magnetized gases or plasmas with $\beta = 8\pi p/B^2$ of order unity, which makes them magnetohydrodynamic (MHD) rather than gasdynamic shocks. Since the uniformity of compression is the key to success for all kinds of ICF, achieving a clear understanding of the stability of these MHD shocks and confident modeling of their response to small perturbations is very important. This is the subject of the present article.

The theory of stability of gasdynamic shock fronts developed from the 1940s–'50s [39–41] is now a mature field of compressible fluid dynamics whose main results are summarized in monographs and textbooks [42–44]. Planar shock fronts in most materials, including ideal gases with any adiabatic exponent γ, are superstable for any shock strength, which means that their shape perturbations decay as a power of time t, specifically, as $t^{-3/2}$ for moderate-strength shocks and $t^{-1/2}$ in the strong-shock limit [45–48]. For some non-ideal equations of state (EoS), in specific ranges of shock strengths, neutral stability is possible under conditions elucidated by D'yakov [40] and Kontorovich [41] (DK), with the perturbed shock front exhibiting nondecaying oscillations that produce spontaneous acoustic emission (SAE) downstream. Planar shock fronts can be exponentially unstable [41–44] when a single-shock solution of the Riemann/piston problem is not unique. In this case, the theory [49,50] predicts that an unstable shock splits into a multiwave flow; see a numerical example in Ref. [51]. The presence of a rigid piston as the boundary condition driving the planar shock does not change the character of the solution [52,53] yet additional frequencies may emerge due to the reflection of sonic waves on the piston surface, subsequently reaching the shock. If the shock driving mechanism is not steady and the associated external excitation frequency aligns with the self-induced oscillation frequency in the SAE regime, then the shock can exhibit unstable behavior [53].

Gardner and Kruskal [54], who extended the formalism developed by Erpenbeck [55] for gasdynamic shocks, started stability studies of MHD shock waves in the 1960s. For fast MHD shocks propagating in parallel and perpendicular directions to the shock front, they demonstrated the absence of exponential instability for an ideal-gas conducting fluid (plasma) with $\gamma < 3$. Later studies, mostly reported in the mathematical literature (cf. Ref. [56] and references therein), were performed exclusively for ideal-gas EoS. They found

the DK ranges of neutral stability and SAE for fast MHD shocks. In Ref. [57] the propagation of fast magnetosonic waves in an inhomogeneous medium with planar flow is investigated. In addition, the study explores the existence of eigenmodes in a steady flow containing a shock. The eigenmodes are used to derive the reflection coefficient of a fast magnetosonic wave from the shock. Recently, particle-in-cell (PIC) simulations have been used to model high-frequency processes in fast magnetosonic shocks, with a particular emphasis on electron dynamics. However, the long-time shock dynamics remain inaccessible due to computational constraints [58].

In this paper, we revisit the MHD shock-front stability problem and construct an analytical model to solve the initial-value problem (IVP) for isolated-shock boundary conditions. Besides, a numerical analysis of perpendicular MHD shocks is carried out. We focus on the perpendicular shocks, which can only be of the fast variety, [59] the kind of particular practical importance for all the above ICF applications. Moreover, we limit ourselves to the usually most unstable interchange instability modes, which do not bend the magnetic force lines. Then, the presence of the frozen-in magnetic field in the shock-compressed fluid translates into a modification of its EoS (cf. Ref. [59], Sec. 52), which makes possible a direct application of the gasdynamic theoretical techniques and stability criteria [40–42]. Our stability analysis is carried out for three equations of state: (1) ideal gas, with the adiabatic exponent γ varied in a broad range; (2) van der Waals (vdW) fluid; (3) a model EoS for simple metals, such as aluminium, used in Ref. [60] to analyze the stability of spherical and cylindrical expanding shock waves. Our results can be summarized as follows. We found a DK range of neutral stability for sufficiently strong shocks in a low-β ideal plasma with $\gamma > 1 + \sqrt{2}$, the magnetic field thereby acting as a destabilizing factor, enabling the SAE. A similar high-γ, low-β neutral stability range is also found for a vdW fluid, which also manifests SAE at low γ, as discovered in Ref. [61]. In the latter case, however, the magnetic field acts as a stabilizer, suppressing the SAE unless β is small enough. The model EoS for simple metals offers a realistic case of high effective γ: metals are nearly incompressible at low shock pressures. However, the DK neutral stability conditions require a finite shock strength, which results in γ decreasing to low values, insufficient to satisfy the DK conditions for neutral stability. This is why the perpendicular MHD shocks in aluminium were found to be stable across the entire range of parameters explored. Our analytical predictions for the perturbation evolution for the ideal-gas EoS were cross-checked with MHD fluid simulations done with the FLASH code [62]. (For more information on the FLASH code, see Ref. [63]). The paper is structured as follows. The mathematical formulation of the fast MHD shock, both base-flow conditions and perturbation variables, is given in Sec. II. The stability limits are presented and discussed in Sec. III for different EoS and shock B intensities. The transient evolution of the shock front and the perturbed variables downstream are described in Sec. IV for an ideal gas EoS, with the former being contrasted against numerical simulations in Sec. V. This section also presents snapshots for the simulated pressure and density fields. Finally, the main conclusions are summarized in Sec. VI.

II. PROBLEM DESCRIPTION

A. Base-flow MHD shock

Let a planar shock front move with velocity $\vec{u}_1 = u_1 \hat{e}_x$ in a uniform medium with known pressure p_1, density ρ_1, and internal energy E_1. Let us consider a magnetic field ahead of the shock $\vec{B}_1 = B_1 \hat{e}_z$ that is perpendicular to the shock propagation direction. In a reference frame attached to the shock front, the conservation equations across the shock discontinuity read as

$$[\rho u] = 0, \tag{1a}$$

$$\left[p + \rho u^2 + \frac{B_t^2}{8\pi} \right] = 0, \tag{1b}$$

$$[B_t u] = 0, \tag{1c}$$

$$\left[\rho u \left(e + \frac{p}{\rho} + \frac{u^2}{2} \right) + u \frac{B_t^2}{4\pi} \right] = 0, \tag{1d}$$

provided that the normal component of the magnetic field, which must be continuous across the shock front, is zero: $B_{x1} = B_{x2} = 0$. In what follows we identify postshock flow variables with the subscript 2.

The formulation benefits from the introduction of the dimensionless functions $\mathcal{P} = p_2/p_1$ and $\mathcal{R} = \rho_2/\rho_1$, which measure the pressure and density jumps across the shock, respectively. Likewise, the characteristic Mach numbers are defined in relation to the characteristic velocities of the linear MHD waves, namely,

$$c_A^2 = \frac{B^2}{4\pi\rho}, \tag{2a}$$

$$c_T^2 = \left. \frac{\partial p}{\partial \rho} \right|_s \tag{2b}$$

for the Alfvén (magnetic) and sonic (thermal) velocities, respectively, with $c_F^2 = c_T^2 + c_A^2$ being used to define the fast magnetosonic velocity. As derived in the following, only the fast magnetosonic velocity is allowed (see Sec. II B for further details), thereby being the characteristic speed to define the shock Mach number. Then, a fast and evolutionary MHD shock is determined by the conditions $\mathcal{M}_{F1} = u_1/c_{F1} > 1$ and $\mathcal{M}_{F2} = u_2/c_{F2} < 1$ on the fast magnetosonic Mach numbers. It is convenient, however, to define the Alfvén Mach numbers as $\mathcal{M}_{A1} = u_1/c_{A1}$ and $\mathcal{M}_{A2} = u_2/c_{A2}$, where the former can be written, with the aid of Eqs. (1a)–(1c), as

$$\mathcal{M}_{A1}^2 = \frac{\beta(\mathcal{P} - 1) + \mathcal{R}^2 - 1}{2(1 - \mathcal{R}^{-1})}, \tag{3}$$

where $\beta = 8\pi p_1/B_1^2$ stands for the preshock plasma β parameter, which measures the thermal pressure relative to the magnetic pressure.

With use made of Eq. (1d), the Hugoniot adiabat reads as $\mathcal{H} = 0$, where

$$\mathcal{H} = \mathcal{E} - \frac{(\mathcal{P} + 1)(\mathcal{R} - 1)}{2\mathcal{R}} - \frac{1}{\beta} \frac{(\mathcal{R} - 1)^3}{2\mathcal{R}}, \tag{4}$$

and where $\mathcal{E} = \rho_1(E_2 - E_1)/p_1$ is appropriately introduced to represent the dimensionless variation of the internal energy across the shock. Therefore, the RH adiabat $\mathcal{H} = 0$ is closed upon determination of the internal energy function,

$\mathcal{E} = \mathcal{E}(\mathcal{R}, \mathcal{P})$, which ultimately renders the RH curve in the form $\mathcal{P} = \mathcal{P}(\mathcal{R})$.

Anticipating that $\mathcal{M}_{F2}$ is a needed function to describe the shock dynamics, an explicit definition is given:

$$\mathcal{M}_{F2}^2 = \frac{\mathcal{M}_{A1}^2}{\mathcal{R}^2} \frac{c_{A1}^2}{c_{F2}^2}$$

$$= \frac{\beta(\mathcal{P} - 1) + \mathcal{R}^2 - 1}{2\mathcal{R}(\mathcal{R} - 1)} \left(\gamma_T \beta \frac{\mathcal{P}}{2\mathcal{R}} + \mathcal{R} \right)^{-1}, \tag{5}$$

where the polytropic index is conveniently introduced for an arbitrary EoS $p = (\rho, T)$ and internal energy function of state $E = (\rho, T)$:

$$\gamma_T = \frac{\rho_2 c_{T2}^2}{p_2}$$

$$= \frac{\rho_2}{p_2} \left. \frac{\partial p_2}{\partial \rho_2} \right|_T + \frac{1}{\rho_2} \left. \frac{\partial p_2}{\partial T_2} \right|_\rho \left. \frac{\partial E_2}{\partial T_2} \right|_\rho^{-1} \left(1 - \frac{\rho_2^2}{p_2} \left. \frac{\partial E_2}{\partial \rho_2} \right|_T \right). \tag{6}$$

B. Linear perturbation analysis

The problem continues with the formulation of the linearized ideal MHD equations that govern the unsteady postshock flow, namely,

$$\frac{\partial \delta\rho}{\partial t} + \rho_2 \boldsymbol{\nabla} \cdot \delta\vec{v} = 0, \tag{7a}$$

$$\rho_2 \frac{\partial \delta\vec{v}}{\partial t} + \boldsymbol{\nabla}\delta p - (\boldsymbol{\nabla} \times \delta\vec{B}) \times \frac{\vec{B}_2}{4\pi} = 0, \tag{7b}$$

$$\frac{\partial \delta p}{\partial t} - c_{T2}^2 \frac{\partial \delta\rho}{\partial t} = 0, \tag{7c}$$

$$\frac{\partial \delta\vec{B}}{\partial t} - \boldsymbol{\nabla} \times (\delta\vec{v} \times \vec{B}_2) = 0, \tag{7d}$$

written in a reference frame comoving with the fluid particles. They correspond to the equation of continuity, the conservation of linear momentum, the conservation of energy for an isentropic and adiabatic flow, and the magnetic induction equation. The parameter c_{T2} corresponds to the speed of sound in the shocked gas. The formulation assumes that the base-flow is uniform, that the medium is a perfect conductor, and that all perturbations are of the same order,

$$\frac{\delta\rho}{\rho_2} = \frac{|\delta\vec{B}|}{|\vec{B}_2|} \sim \frac{\delta p}{p_2} \sim \frac{|\delta\vec{v}|}{c_{T2}} \sim \epsilon \ll 1, \tag{8}$$

with ϵ being the small parameter that identifies the amplitude of the perturbations. In our case, it is determined by the initial small shock corrugation amplitude $\epsilon\lambda = \psi_s(t = 0) = \psi_{s0}$ scaled with the corrugation wavelength (see sketch depicted in Fig. 1).

For the particular case considered in this work, the magnetic field points in the direction perpendicular to the plane $\delta\vec{B}/|\delta\vec{B}| = \vec{B}_2/|\vec{B}_2| = \hat{e}_z$, while velocity perturbations sit on the plane $\{\hat{e}_x, \hat{e}_y\}$. Then, with use made of $\delta\vec{v}(x, y) \cdot \vec{B}_2(x, y) = 0$, the governing equation for the perturbed velocity field reads as

$$\frac{\partial^2 \delta\vec{v}}{\partial t^2} = c_{F2}^2 (\nabla^2 \delta\vec{v} + \boldsymbol{\nabla} \times \boldsymbol{\nabla} \times \delta\vec{v}), \tag{9}$$
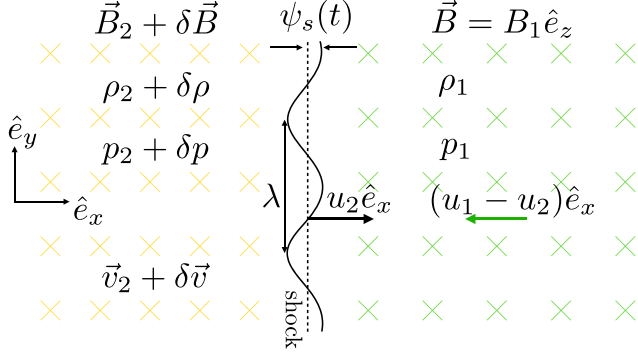
FIG. 1. Sketch of the corrugated perpendicular shock moving through the magnetized medium whose magnetic field points perpendicular to the shock propagation direction and to the velocity disturbances. Velocities are measured in the postshock gas reference frame ($\bar{v}_2 = 0$).

where $\delta\vec{v}(x, y, t)$ accounts for both fast magnetoacoustic $\delta\vec{v}_F$ and rotational $\delta\vec{v}_r$ contributions, which satisfy $\nabla \times \delta\vec{v}_F = 0$ and $(\partial\vec{v}_r)/(\partial t) = 0$, respectively. Note that Eq. (9) can be written for each velocity component (longitudinal and transverse) independently, a simplification that is not possible when $\delta\vec{v}(x, y) \cdot \vec{B}_2(x, y) \neq 0$ because the three modes of propagation (Alfvén, slow and fast magnetosonic waves) involve coupled information of the three dimensions.

Simple manipulation allows us to write Eq. (9) in terms of the total pressure $p_2^* = p_2 + B_2^2/(8\pi)$, which accounts for the thermal plus the magnetic contributions, in the following form:

$$\frac{\partial^2 \delta p^*}{\partial t^2} = c_{F2}^2 \nabla^2 \delta p^*, \tag{10}$$

where

$$\delta p^* = \delta p + \frac{B_2}{4\pi} \delta B \tag{11}$$

indicates the total pressure perturbation. It is readily seen that Eq. (10) corresponds to a conventional sound wave equation, with the distinctiveness that information travels at the so-called fast magnetosonic velocity in the compressed medium, namely, c_{F2}. Therefore, owing to the relative orientation between the shock and the magnetic field, our linearized MHD equations only involve the characteristic velocity c_{F2}, which is used to nondimensinalize the spatiotemporal variables in the form $\tau = kc_{F2}t$ and $(\bar{x}, \bar{y}) = k(x, y)$, where $k = 2\pi/\lambda$ is the wave-number frequency. Likewise, the dimensionless order-of-unity shock ripple amplitude is defined, along with the corresponding postshock perturbation variables, as follows:

$$\frac{1}{\epsilon} \frac{\psi(\bar{x}, \bar{y}, \tau)}{\psi_{s0}} = \bar{\xi}(\bar{x}, \tau) \cos(\bar{y}), \tag{12a}$$

$$\frac{1}{\epsilon} \frac{\delta p^*(\bar{x}, \bar{y}, \tau)}{\rho_2 c_{F2}^2} = \bar{p}^*(\bar{x}, t) \cos(\bar{y}), \tag{12b}$$

$$\frac{1}{\epsilon} \frac{\delta u(\bar{x}, \bar{y}, \tau)}{c_{F2}} = \bar{u}(\bar{x}, \tau) \cos(\bar{y}), \tag{12c}$$

$$\frac{1}{\epsilon} \frac{\delta v(\bar{x}, \bar{y}, \tau)}{c_{F2}} = \bar{v}(\bar{x}, \tau) \sin(\bar{y}), \tag{12d}$$

$$\frac{1}{\epsilon} \frac{\delta\rho(\bar{x}, \bar{y}, \tau)}{\rho_2} = \bar{\rho}(\bar{x}, \tau) \cos(\bar{y}), \tag{12e}$$

$$\frac{1}{\epsilon} \frac{\delta B(\bar{x}, \bar{y}, \tau)}{B_2} = \bar{B}(\bar{x}, \tau) \cos(\bar{y}), \tag{12f}$$

to be used, along with Eq. (7) or Eq. (10), to write

$$\frac{\partial^2 \bar{p}^*}{\partial\tau^2} = \frac{\partial^2 \bar{p}^*}{\partial\bar{x}^2} - \bar{p}^* \tag{13}$$

as a parameter-free transverse-periodic sound wave equation that calls for two initial conditions and two boundary conditions in the streamwise direction.

One boundary condition is determined by the linearized shock conservation equations, written in dimensionless form as

$$\frac{d\xi_s}{d\tau} = \frac{1 + h^*}{2\mathcal{M}_{F2}} \frac{\mathcal{R}}{\mathcal{R} - 1} \bar{p}_s^*, \tag{14a}$$

$$\bar{u}_s = \frac{1 - h^*}{2\mathcal{M}_{F2}} \bar{p}_s^*, \tag{14b}$$

$$\bar{v}_s = -\mathcal{M}_{F2}(\mathcal{R} - 1) \frac{\partial\xi_s}{\partial\bar{y}}, \tag{14c}$$

where

$$h^* = \frac{p_2^* - p_1^*}{V_1 - V_2} \left(\frac{dp_2^*}{dV_2}\right)_H^{-1} \tag{15}$$

corresponds to the redefined DK parameter, which measures the slope of the RH curve as relative to the Rayleigh-Michelson line in the $\{p^*, V = 1/\rho\}$ plane. Note that, as with regular nonmagnetized shocks, the formulation of the linear problem is described in terms of three dimensionless parameters: the shock compression ratio $\mathcal{R}$, the postshock Mach number $\mathcal{M}_{F2}$, and the RH slope parameter h^*. The perturbation in the magnetic field intensity is dictated by the conservation of the magnetic flux across the shock $B_1 u_1 = B_2 u_2$ to yield $\bar{\rho}_s = \bar{B}_s$, where density perturbations behind the shock follows:

$$\bar{\rho}_s = -\frac{h^*}{\mathcal{M}_{F2}^2} \bar{p}_s^*, \tag{16}$$

as dictated by the perturbation of the RH curve. The other boundary condition is determined by the supporting mechanism. For the isolated-shock condition considered in this work, the condition reduces to omitting the effect of the magnetosonic waves reaching the shock from behind, which is a valid assumption when the shock is sufficiently far from the supporting mechanism. As for the initial conditions, we can assume that the shock is initially distorted: $\xi_{s0} - 1 = \bar{p}_{s0}^* = 0$.

Note that for our perpendicular shock geometry, as noted in Sec. 52 of Ref. [59] citing Ref. [64] (see also Ref. [65]), the one-dimensional MHD equations reduce to the equations of the ordinary fluid dynamics, with a modified equation of state in which the thermal pressure p is replaced by $p^* = p + B^2/(8\pi) = p + \text{const } \rho^2$. This simplification remains valid in our two-dimensional MHD stability problem for the interchange perturbation modes that do not bend the magnetic force lines. In the following, we demonstrate how the above modification of the equation of state due to the frozen-in magnetic field affects the stability of the shock front.

III. STABILITY LIMITS

A shock wave is said to be stable if any perturbation at the shock front decays with time. The condition for stability is typically written in terms of the DK parameter h through the inequality $-1 < h < h_c$, where h_c corresponds to its critical value [59]. The stability condition can be easily extrapolated from nonconducting shocks to fast magnetosonic shocks, with the magnetic field being parallel to the shock front, by just redefining the parameters $h = h^*$ and

$$h_c^* = \frac{1 - M_{F2}^2(1 + \mathcal{R})}{1 - M_{F2}^2(1 - \mathcal{R})}. \quad (17)$$

The DK parameter is conveniently rewritten as a function of dimensionless variables as

$$h^* = -\frac{(\mathcal{P} - 1)\beta + \mathcal{R}^2 - 1}{(\beta + 1)\mathcal{R}(\mathcal{R} - 1)}\left(\frac{d\mathcal{P}^*}{d\mathcal{R}}\right)^{-1} \quad (18)$$

$$= -\frac{(\mathcal{P} - 1)\beta + \mathcal{R}^2 - 1}{\beta\mathcal{R}(\mathcal{R} - 1)}\left(\frac{d\mathcal{P}}{d\mathcal{R}} + \frac{2\mathcal{R}}{\beta}\right)^{-1},$$

where

$$\mathcal{P}^* = \frac{p_2^*}{p_1^*} = \frac{\beta\mathcal{P} + \mathcal{R}^2}{\beta + 1} \quad (19)$$

represents the ratio of the total pressures across the shock. The slope of the dimensionless thermal pressure with respect to the density compression ratio can be obtained using the Hugoniot expression (4), namely,

$$\frac{d\mathcal{P}}{d\mathcal{R}} = -\frac{\partial\mathcal{H}}{\partial\mathcal{R}}\left(\frac{\partial\mathcal{H}}{\partial\mathcal{P}}\right)^{-1} \quad (20)$$

$$= \frac{1 + 2\mathcal{R}^3 + \beta + \mathcal{P}\beta - \mathcal{R}^2(3 + 2\mathcal{E}_R\beta)}{\mathcal{R}\beta + (-1 + 2\mathcal{E}_P\mathcal{R}\beta)},$$

where $\mathcal{E}_R = \partial\mathcal{E}/\partial\mathcal{R}|_{\mathcal{P}}$ and $\mathcal{E}_P = \partial\mathcal{E}/\partial\mathcal{P}|_{\mathcal{R}}$ correspond to the partial derivatives of the internal energy variation function. Equation (20), and therefore the DK parameter h^*, requires the information about the internal energy function of state. However, the function h_c^* calls for information on the equation of state through the definition of the postshock magnetosonic Mach number.

In the stable regime, $-1 < h^* < h_c^*$, perturbations at the shock front experience a decay that follows a $\tau^{-3/2}$ pattern in the long-time $\tau \gg 1$. However, there exists a subregime where perturbations experience an exponential decay in the early-time stages $\tau \lesssim 1$, although the long-time is still being dominated by the power law $\tau^{-3/2}$; see Refs. [66,67]. This is given by the condition $-1 < h^* < h_d^*$, where

$$h_d^* = \frac{\left(1 - \mathcal{M}_{F2}^2\right)^{3/2}\sqrt{1 - \mathcal{R}^{-1}} - \mathcal{R}\mathcal{M}_{F2}^2}{1 + \mathcal{M}_{F2}^2(\mathcal{R} - 1)}. \quad (21)$$

In the context of this study, it is important to investigate whether the magnetic field can be used to induce an initial strong damping of perturbations in the shock, $h^* < h_d^*$,

placing it in the regime where perturbations are subsequently effectively suppressed. Recall that such strong damping is impossible in a nonmagnetized ideal gas EoS for any γ. In the following, the parameters defined above are evaluated with different EoS associated with an ideal gas, a vdW gas and an aluminium three-term EoS.

A. Ideal gas equation of state

The particularization to an ideal gas is relatively simple. The corresponding constitutive equations for pressure and internal energy (assumed to be calorically perfect) are $p = R_g\rho T$ and $E = c_v T$, respectively, where $R_g = c_p - c_v$ is the gas constant and $\gamma = c_p/c_v$ is the specific heats ratio. Simple manipulation renders

$$\mathcal{E} = \frac{1}{\gamma - 1}\left(\frac{\mathcal{P}}{\mathcal{R}} - 1\right) \text{ and } \gamma_T = \gamma, \quad (22)$$

which allows us to write the RH curve in explicit form

$$\mathcal{P} = \frac{\mathcal{R}(\gamma + 1) - (\gamma - 1)}{(\gamma + 1) - \mathcal{R}(\gamma - 1)} + \frac{1}{\beta}\frac{(\mathcal{R} - 1)^3(\gamma - 1)}{(\gamma + 1) - \mathcal{R}(\gamma - 1)}, \quad (23)$$

where the first term on the right-hand side is easily recognizable as the adiabatic nonmagnetized pressure jump across the shock. The second term accounts for the magnetic contribution that drops to zero when $\beta \to \infty$.

The effect of the magnetic field in the pressure jump is better analyzed with the aid of Fig. 2, which shows the Rankine-Hugoniot curves for a MHD shock with different values of the transverse magnetic field intensities. Both thermal $\mathcal{P}$ (a) and thermal-plus-magnetic $\mathcal{P}^*$ (b) pressure ratios are represented on the left and right panels, respectively. Note that $\mathcal{R}^{\max} = (\gamma + 1)/(\gamma - 1)$ does not depend on the plasma parameter β and it yields $(\mathcal{R}^{-1})_{\min} = 1/4$ for $\gamma = 5/3$. It is also observed that the thermal contribution dominates for sufficiently strong shocks as a result of the bounded limit of the magnetic contribution, given by the maximum density compression ratio $(B_2^2/B_1^2)_{\max} = (\mathcal{R}^2)_{\max} = 16$ for $\gamma = 5/3$.

From a simple inspection of Fig. 2, it is difficult to anticipate the possibility of DK instability since the slope of the RH curve for $\mathcal{P}^*$ does not exhibit any peculiar behavior: the curve monotonically approaches the asymptote predicted by the the maximum density compression ratio. Similar computations for lower and higher values of γ do not change this qualitative behavior. To compute the DK parameter h^* that ultimately determines the stability we must specify the value of the partial derivatives of the internal energy function, namely,

$$\mathcal{E}_R = \left.\frac{\partial\mathcal{E}}{\partial\mathcal{R}}\right|_{\mathcal{P}} = -\frac{\mathcal{P}}{\mathcal{R}^2(\gamma - 1)}, \quad (24a)$$

$$\mathcal{E}_P = \left.\frac{\partial\mathcal{E}}{\partial\mathcal{P}}\right|_{\mathcal{R}} = \frac{1}{\mathcal{R}(\gamma - 1)}, \quad (24b)$$

to provide

$$h^* = -\frac{[-1 + \mathcal{R}(-1 + \gamma) - \gamma][\mathcal{R}(-2 + \gamma) - (1 + \beta)\gamma]}{\mathcal{R}[-2 + 2\mathcal{R}(2 + \mathcal{R}) + \gamma + (2 - 3R)R\gamma + 2\beta\gamma + (-1 + \mathcal{R})^2\gamma^2)]} \quad (25)$$
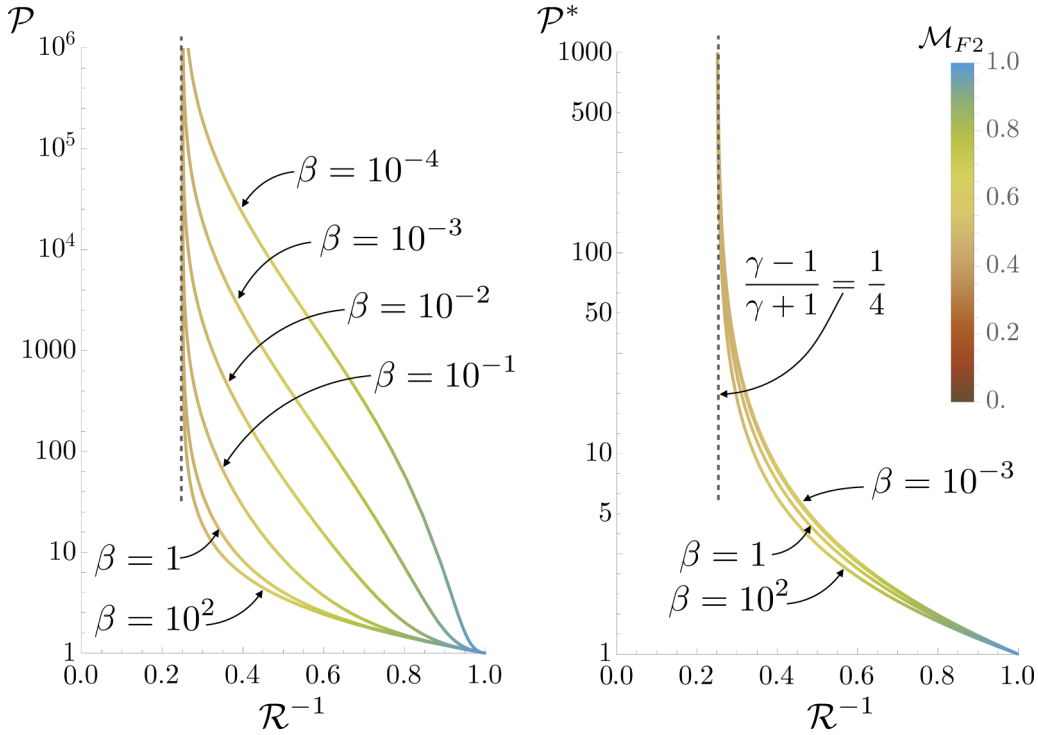
FIG. 2. Rankine-Hugoniot curves for an MHD shock in an ideal gas with different values of transverse magnetic field intensities. The adiabatic index is $\gamma = 5/3$.

as an explicit function of γ, β, and $\mathcal{R}$. The critical parameter h_c^*, however, calls for the determination of the fast magnetosonic Mach number

$$\mathcal{M}_{F2}^2 = \frac{2(2\mathcal{R} + \gamma - \mathcal{R}\gamma + \beta\gamma)}{2\mathcal{R}^2(1 + \mathcal{R}) + \gamma + 3\gamma\mathcal{R}[(5/3 - \mathcal{R})R - 1] + (\mathcal{R} - 1)^3\gamma^2 + \beta[\gamma + \mathcal{R}\gamma + (\mathcal{R} - 1)\gamma^2]}, \tag{26}$$

to be used in Eq. (17) to yield

$$h_c^* = \frac{[\mathcal{R}(\gamma - 1) - (\gamma + 1)][\gamma(\mathcal{R} - 1)^2 + \beta\gamma - 2(\mathcal{R} - 2)\mathcal{R}]}{2\mathcal{R}[\mathcal{R}(3 + \mathcal{R}) - 2] + [\mathcal{R}(1 - 3(\mathcal{R} - 1)\mathcal{R} + 3\beta) - (\beta + 1)]\gamma + (\mathcal{R} - 1)[(\mathcal{R} - 1)^2 + \beta]\gamma^2}. \tag{27}$$

The DK stability can be determined by evaluating the function $h^* - h_c^*$, which depends on γ, β, and $\mathcal{R}$. When $h^* - h_c^* > 0$, the shock front, assumed to be isolated, will oscillate with constant amplitude and constant frequency in the long time regime. Figure 3 shows $h^* - h_c^*$ as a function of the inverse of the density compression ratio $\mathcal{R}^{-1}$ for different values of the adiabatic exponent γ and the preshock plasma parameter β. We vary γ from a low value of $\gamma = 4/3$, which in the shock stability studies is physically associated with strongly radiating gases [68,69] to the high value of $\gamma = 4$ indicating low shock compressibility; γ's in this range are used for a simplified theoretical description of shocks in condensed materials, from $\gamma = 3$ in Refs. [39,70] to $\gamma = 7$ in Ref. [71]. The plasma parameter is varied between $\beta = 10^3$ and $\beta = 10^{-3}$, which correspond to the limits of negligible and dominant, respectively, contributions of the magnetic pressure to the preshock value of p^*.

The stability properties of nonmagnetized shock fronts in ideal gases are independent of the adiabatic exponent γ. In particular, ideal-gas shock fronts do not exhibit the DK instability, which produces spontaneous acoustic emission (SAE),

at any γ. Similarly, the time evolution of shock ripples does not include the early phase of fast exponential decay, as predicted by Ref. [66] for the DK parameter sufficiently close to -1; see in the following. Here we demonstrate that the effective modification of the EoS of the shocked material by the frozen-in magnetic field changes this. Depending on the values of γ, β and the shock strength, the magnetization can act either as a destabilizing factor, enabling the SAE, or as a stabilizing factor, producing the early-time exponential decay of the shock-front ripples.

The DK instability condition $h^* > h_c^*$ is found to occur in low compressible, highly magnetized plasma. Note that, for $\gamma = 2$, the magnetic field does not influence the shock conditions for any compression ratio. In particular, $h^*(\gamma = 2) = (\mathcal{R} - 3)/(2\mathcal{R})$ and $h_c^*(\gamma = 2) = (\mathcal{R} - 3)/(5\mathcal{R} - 3)$. This is indeed indicative of a change in the character of the solution, since for $\gamma > 2$ the curve with lower β takes higher positions, as opposed to cases where $\gamma < 2$. However, $\gamma > 2$ is not a sufficient condition for instability, as shown in Fig. 3. Although the magnetic effect toward instability changes its character for $\gamma > 2$, its contribution must overcome the stabilizing acoustic
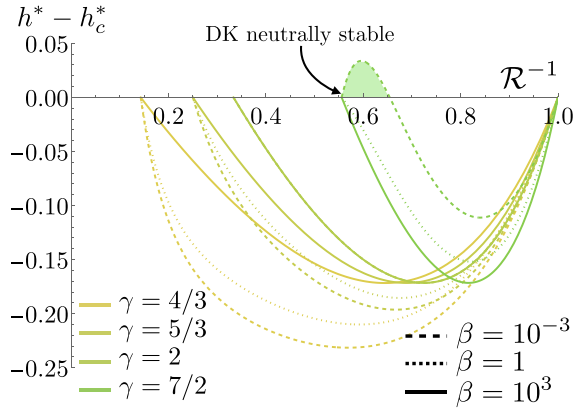
FIG. 3. Function $h^* - h_c^*$ as a function of $\mathcal{R}^{-1}$ for different values of the transverse magnetic intensity β and the adiabatic index γ.

counterpart. This is better analyzed by evaluating the slope of the function $h^* - h_c^*$ in the strong-shock limit, namely,

$$
\bar{h}_{\mathcal{R}}^* = \frac{d(h^* - h_c^*)}{d(\mathcal{R}^{-1})}\bigg|_{\mathcal{R} = \frac{\gamma+1}{\gamma-1}} \tag{28}
$$

$$
= -\frac{(1+\gamma)}{4(\gamma-1)}\frac{2 + [4 + \beta(\gamma-1)^2 - 2\gamma]\gamma}{2 + \beta(\gamma-1)\gamma},
$$

which is found to approach zero in a strongly magnetized plasma $\beta \ll 1$ when $\gamma = 1 + \sqrt{2}$. Since the slope $\bar{h}_{\mathcal{R}}^*$ is a monotonic function of β, the stability regimes are easily identified in an ideal gas: for $\gamma > 1 + \sqrt{2}$, a sufficiently small

value of β will render SAE in the strong-shock limit, while stability is ensured for $\gamma < 1 + \sqrt{2}$.

Akin to h_c^* in Eq. (27), the DK parameter value that distinguishes the regime in which perturbations may decay exponentially in the early time, h_d^*, can be easily expressed in terms of the parameters $\mathcal{R}$, γ, and β by direct substitution of Eq. (26) into Eq. (21). However, since this expression is objectively long, we omit writing the explicit relationship of h_d^* for an ideal gas EoS.

The distinguished regimes that characterize the long-time response of the perturbed shock are better analyzed by looking at Fig. 4, which shows the isocontours $h^* = h_d^*$ (a) and $h^* = h_c^*$ (b) as a function of the shock compression ratio $\mathcal{R}$ and the parameter β for different values of the adiabatic index γ. Observing first the isocurves $h^* = h_d^*$, the state in which a perturbed shock initially develops with rapid exponential damping ($h^* < h_d^*$) is characterized by the region below the inverted U-shaped curve, namely for any shock strength below $\mathcal{R}^{\max}$ when the magnetic field is sufficiently strong. We recall that the magnetic field has a stabilizing effect only for values of γ that are less than 2. Examining Fig. 4(b) and focusing on the isocurves where $h^* = h_c^*$ instead, it is evident that the region of neutral stability/SAE regime ($h^* > h_c^*$) is located beneath the L-shaped curve associated with magnetic fields of significant strength within a limited range of shock compression ratios. Note that this phenomenon occurs in cases where the adiabatic indices are high, as the magnetic field only has a destabilizing effect for values of γ greater than 2. For clarity purposes, Fig. 4 also displays, with the diamond and star symbols, the conditions under which Figs. 8 and 11 are computed.
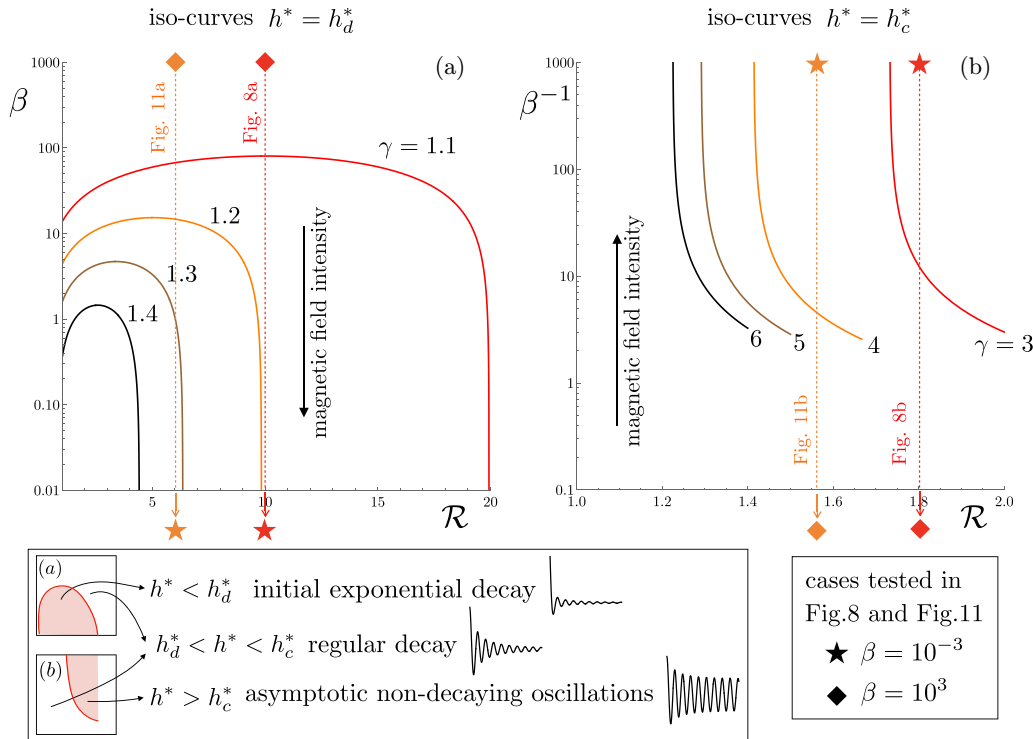

FIG. 4. Isocurves for $h^* = h_d^*$ (a) and $h^* = h_c^*$ (b) as a function of shock compression ratio $\mathcal{R}$ and the parameter β for different values of the adiabatic index.

B. Van der Waals equation of state

The vdW EoS provides a more accurate description of real fluid behavior than the ideal gas law. It takes into account the effect associated with the noncontact interaction between particles and the finite volume they occupy. This EoS is particularly interesting because it is known to lead to DK instability for sufficiently compressible flows, as found in Refs. [60,61,72] for a regular gasdynamic shock. To study the stability boundary of the vdW magnetized gas, we need to explicitly define the corresponding EoS $p(\rho, T)$ and internal energy relationship $E(\rho, T)$, namely,

$$p = \frac{\rho R_g T}{1 - b' \rho} - a' \rho^2, \tag{29a}$$

$$E = \frac{R_g T}{\gamma - 1} - a' \rho, \tag{29b}$$

respectively. With respect to the ideal gas EoS, the term involving the constant a' corrects for the intermolecular attraction, while b' represents the volume occupied by the gas particles (covolume). It is readily seen that Eq. (29) reduces to the ideal gas model when a' and b' approach zero, namely $p = \rho R_g T$ and $E = R_g T / (\gamma - 1)$.

To solve the RH equations, it proves convenient to write the internal energy and the speed of sound as functions of p and ρ

by direct combination of the two relationships in Eq. (29) and the definition of the speed of sound, resulting in

$$E = \frac{(p + \rho^2 a')(1 - b' \rho)}{\rho(\gamma - 1)} - a' \rho, \tag{30a}$$

$$c^2 = \frac{\gamma(p + \rho^2 a')}{\rho(1 - b' \rho)} - 2a' \rho, \tag{30b}$$

respectively. Simple manipulation of Eq. (30) provides $c^2 = \gamma R_g T = \gamma p / \rho$ as the square of the speed of sound for an ideal gas EoS, i.e., $a' = b' = 0$. In dimensionless form, the gain of internal energy reads as

$$\mathcal{E} = \frac{(\mathcal{P} + \mathcal{R}^2 a)(1 - b\mathcal{R}) - \mathcal{R}(1 + a)(1 - b)}{\mathcal{R}(\gamma - 1)} - a(\mathcal{R} - 1), \tag{31}$$

and the polytropic index needed to define the postshock Mach number $\mathcal{M}_{F2}$ in Eq. (5) is

$$\gamma_T = \gamma \frac{\mathcal{P} + \mathcal{R}^2 a}{\mathcal{P}(1 - b\mathcal{R})} - 2a \frac{\mathcal{R}^2}{\mathcal{P}}, \tag{32}$$

where $a = a' \rho_1^2 / p_1$ and $b = b' \rho_1$ are dimensionless parameters of the vdW EoS.

The RH relationship for a magnetized vdW gas can be expressed explicitly using the dimensionless internal energy gain factor $\mathcal{E}$, as follows:

$$\mathcal{P} = \frac{\mathcal{R}[\gamma + 1 - 2b(a+1) - 2a(\gamma - 2)] - (\gamma - 1) + 2a\mathcal{R}^2(\gamma - 2 + b\mathcal{R})}{(\gamma + 1) - \mathcal{R}(\gamma - 1 + 2b)} + \frac{1}{\beta} \frac{(\mathcal{R} - 1)^3(\gamma - 1)}{(\gamma + 1) - \mathcal{R}(\gamma - 1 + 2b)}, \tag{33}$$

which is appropriately expressed as the sum of the nonmagnetic and magnetic contributions.

Figure 5 shows the Rankine-Hugoniot curves for an MHD shock in a vdW gas with different values of transverse magnetic field intensity. The selected values for the preshock and vdW EoS parameters correspond to those used in Refs. [60,61] for nonmagnetic shocks associated with high gas compressibility $\gamma = 31/30$, nonnegligible vdW parameters, $a = 1/2$ and $b = 1/9$, since they render the DK instability $h > h_c$ within an interval of shock strengths corresponding to $2.2586 < \mathcal{R} < 3.1482$. Both thermal $\mathcal{P}$ (a) and thermal-plus-magnetic $\mathcal{P}^*$ (b) pressure ratios are represented in the left and right panels, respectively. The effect of the magnetic field is qualitatively similar to that observed in Fig. 2 for an ideal gas: the thermal contribution dominates for sufficiently strong shocks, since the magnetic contribution is bounded by the maximum density compression ratio $(B_2^2/B_1^2)_{\max} = (\mathcal{R}^2)_{\max} \sim 63$, although this contribution is now higher than that found in the previous case due to the high compressibility of the gas chosen for the computation.

The two partial derivatives required to define the DK parameter h^*, according to Eq. (18), take the form

$$\mathcal{E}_R = \frac{\mathcal{P} + \mathcal{R}^2 a(2\mathcal{R}b + \gamma - 2)}{\mathcal{R}^2(1 - \gamma)}, \tag{34a}$$

$$\mathcal{E}_P = \frac{1 - \mathcal{R}b}{\mathcal{R}(\gamma - 1)}, \tag{34b}$$

for the isochoric and isobaric derivatives, respectively. The functions $\mathcal{P}$, $\mathcal{E}$, γ_T, $\mathcal{E}_R$, and $\mathcal{E}_P$ are used to define h^* and h_c^* as a function of the density compression ratio $\mathcal{R}$ and the constitutive gas parameters γ, a, and b, and the preshock β parameter. For example, Fig. 6 shows the difference $h^* - h_c^*$ as a function of $\mathcal{R}^{-1}$ for different values of the transverse magnetic intensity β and the adiabatic index γ. The vdW parameters are fixed at $a = 1/2$ and $b = 1/9$, respectively. For these particular conditions, the perturbed shock can lead to DK instability for two different reasons: purely acoustic instability (solid orange curve), previously found in Refs. [60,61], and magnetosonic instability (dashed green curve).

As shown previously when studying the ideal gas case, the effect of the magnetic field is stabilizing for sufficiently low values of γ. In the case shown in Fig. 6 for $\gamma = 31/30$, order of unity values of β make the shock stable. Further computations show that β must be less than 63.88 for the shock to be stable for any shock intensity, which was neutrally stable in a nonmagnetized vdW gas with $\gamma = 31/30$, $a = 1/2$, and $b = 1/9$. The effect of the magnetic field is reversed for higher values of γ. Qualitatively similar to what is found in ideal gases, the magnetic field promotes instability in gases with high adiabatic index; see the case with $\gamma = 7/2$ in Fig. 6. One evident distinction is that, for a vdW gas, there is no possibility to get a β-independent configuration, as occurred for $\gamma = 2$ in an ideal gas. Another marked difference is that, since $h^* - h_c^*$ is not zero in the strong-shock limit, the instability prerequisite obtained for ideal gases, $\bar{h}_{\mathcal{R}}^* > 0$, does not apply
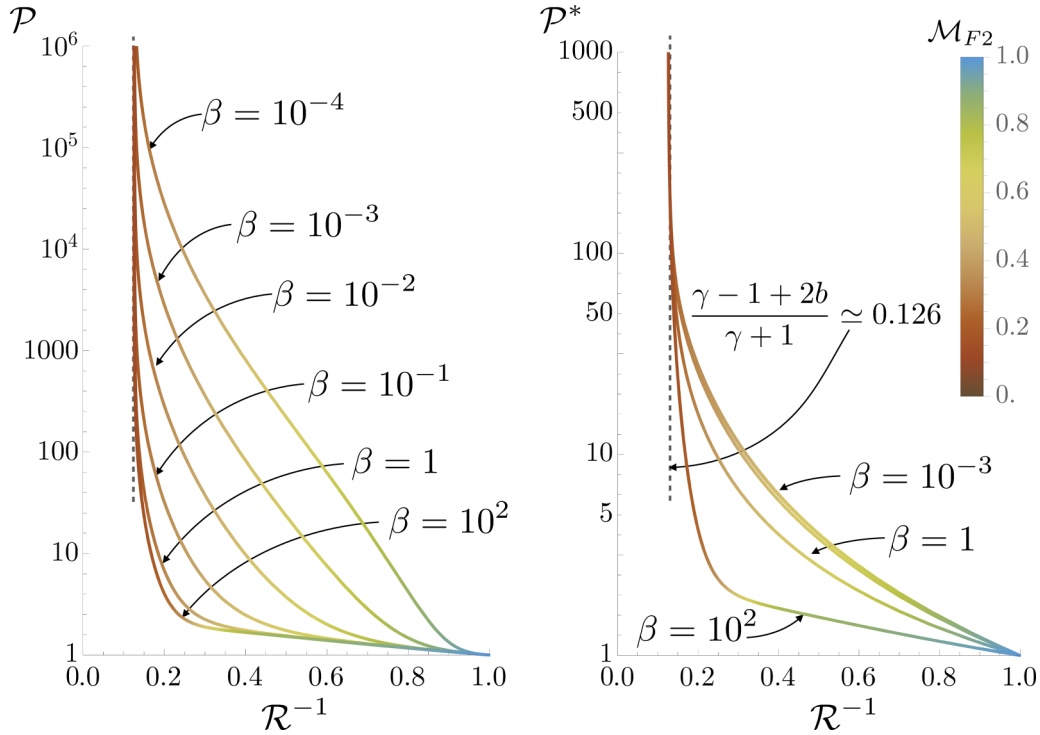
FIG. 5. Rankine-Hugoniot curves for an MHD shock in a vdW gas with different values of transverse magnetic field intensities. The vdW gas parameters are $\gamma = 31/30$, $a = 1/2$, and $b = 1/9$.

in this case, since $\bar{h}_{\mathcal{R}} > 0$ and $h^* - h_c^* < 0$ is still possible for $1 \leqslant \mathcal{R} \leqslant \mathcal{R}^{\mathrm{max}}$.

C. Three-term equation of state for simple metals

In the previous section it was shown that magnetic fields can promote instability under strong-shock conditions for gases whose adiabatic index is sufficiently high, $\gamma > 1 + \sqrt{2}$ for an ideal gas EoS. It corresponds to characteristic values for metallic materials, so it is advisable to compute now the stability limits with a more accurate description of the EoS. Recall that ideal-gas equations of state with high γ are often used to approximate the realistic EoS of condensed materials [39,70,71] whose shock compression is low compared to ideal

FIG. 6. Function $h^* - h_c^*$ as a function of $\mathcal{R}^{-1}$ for different values of the transverse magnetic intensity β and the adiabatic index γ. The parameters of the van der Waals EoS are $a = 1/2$ and $b = 1/9$.

gases. However, the assumption of a constant γ independent of the shock strength may be an oversimplification for our shock-front stability studies. In reality, the effective γ defined by Eq. (6) as $\gamma = \partial \ln \mathrm{p} / \partial \ln \rho|_s$ in condensed materials can be large, indicating near-incompressibility for relatively low shock pressures, see the inset in Fig. 7. However, it decreases rapidly with increasing shock compression. Since the DK instability is only possible for finite shock strengths, in this Section we check if the high γ required for the DK instability range in a magnetized material can be produced in shock-compressed solid materials.

For this purpose, we use, as an example, a convenient, analytically tractable three-term EoS based on the cold-pressure approximation developed by Ref. [73]. This model is reasonably accurate in describing the shock compression of simple metals, such as Al and Cu (in this example, we use the parameters for Al, see the Appendix), for shock compressions up to ~2.5 and pressures up to ~5 Mbar. We do not seek higher EoS model accuracy, which can be achieved with more elaborate approximations, such as the seven-parameter model used by Ref. [74]. The reason is that the magnetic fields required to affect the shock compression significantly are too large to be practically compatible with a uniform magnetization of a material in a cold-metal state. The Mbar shock pressure range required for substantial shock compression corresponds to magnetic fields above 5MG, only produced in the laboratory with magnetocumulative generators [75,76]. Interaction of a conducting metal sample with a magnetic field rapidly increased to a multi-MG level results in the explosion of the skin layer, converting the metal into a plasma. Our goal is more straightforward: to check if the increase in effective γ compatible with a realistic EoS of metal can enable SAE
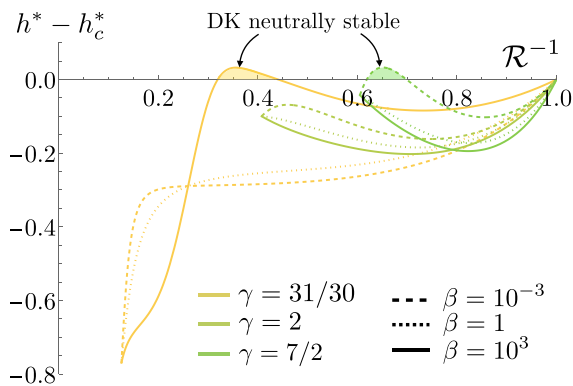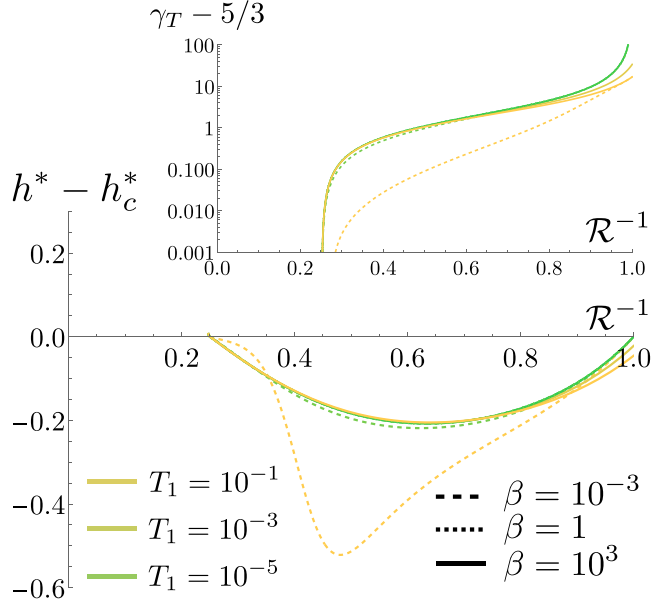
FIG. 7. Function $h^* - h_c^*$ as a function of $\mathcal{R}^{-1}$ for different values of the transverse magnetic intensity β and the upstream temperature (in eV). The scaled upstream density is $z_1 = 1$, corresponding to $\rho_1 = \rho_{0m}$. The inset shows the effective postshock polytropic index as a function of the shock compression ratio.

in magnetized but otherwise DK-stable materials [60]. We demonstrate in the following that this is not the case.

In condensed materials, the equation of state and the internal energy function are typically written in terms of density ρ and temperature T, as described in Eq. (A2) in the Appendix. Then the definition of the parameter h^* through the RH slope $d\mathcal{P}/d\mathcal{R}$ is conveniently expressed in the form

$$\frac{d\mathcal{P}}{d\mathcal{R}} = -\frac{\partial \mathcal{H}}{\partial \mathcal{R}}\left(\frac{\partial \mathcal{H}}{\partial \mathcal{P}}\right)^{-1} = \mathcal{P}'_{\mathcal{R}} - \left.\frac{\partial \mathcal{H}}{\partial \mathcal{R}}\right|_{\mathcal{T}} \left.\frac{\partial \mathcal{H}}{\partial \mathcal{T}}\right|_{\mathcal{T}}^{-1} \mathcal{P}'_{\mathcal{T}}, \quad (35)$$

where $\mathcal{T} = T_2/T_1$ is the temperature ratio across the shock and the functions of the partial derivatives for the EoS and the internal energy are

$$\mathcal{P}'_{\mathcal{R}} = \left.\frac{\partial \mathcal{P}}{\partial \mathcal{R}}\right|_{\mathcal{T}}, \qquad \mathcal{P}'_{\mathcal{T}} = \left.\frac{\partial \mathcal{P}}{\partial \mathcal{T}}\right|_{\mathcal{R}}, \qquad (36a)$$

$$\mathcal{E}'_{\mathcal{R}} = \left.\frac{\partial \mathcal{E}}{\partial \mathcal{R}}\right|_{\mathcal{T}}, \qquad \mathcal{E}'_{\mathcal{T}} = \left.\frac{\partial \mathcal{E}}{\partial \mathcal{T}}\right|_{\mathcal{R}}, \qquad (36b)$$

respectively, with the latter two being used to define the partial derivatives along the Hugoniot, namely,

$$\left.\frac{\partial \mathcal{H}}{\partial \mathcal{R}}\right|_{\mathcal{T}} = \frac{2\mathcal{R}\mathcal{E}'_{\mathcal{R}} - (\mathcal{R}-1)\mathcal{P}'_{\mathcal{R}}}{2\mathcal{R}}$$
$$+ \frac{1 + \beta - 3\beta\mathcal{P} - 3\mathcal{R}^2 + 2\mathcal{R}^3}{2\beta\mathcal{R}^2}, \qquad (37a)$$

$$\left.\frac{\partial \mathcal{H}}{\partial \mathcal{T}}\right|_{\mathcal{R}} = \frac{2\mathcal{R}\mathcal{E}'_{\mathcal{T}} - (\mathcal{R}-1)\mathcal{P}'_{\mathcal{T}}}{2\mathcal{R}}. \qquad (37b)$$

The prime symbols are used here to distinguish $\mathcal{E}'_{\mathcal{R}}$, applied along the isothermal condition, from the one previously defined, $\mathcal{E}_{\mathcal{R}}$, applied along the isobar. The rest of the primed

symbols are kept for consistency. To compute the fast magnetosonic Mach number $\mathcal{M}_{F2}$ needed for the definition of h_c^*, the polytropic index must be provided. It can be computed with the aid of

$$\gamma_T = \frac{\gamma_c p_c + \gamma_l p_l + \gamma_e p_e}{p_c + p_l + p_e}, \qquad (38)$$

which accounts for the cold, lattice, and electronic contributions: γ_c, γ_l, and γ_e, respectively. They are provided in Eq. (A11). Note that γ_T diverges in cold conditions, but it tends to 5/3 if temperature is sufficiently high, as occurs in the gas behind high-intensity shocks.

Figure 7 shows that the shock is stable for all conditions considered: from weak to intense magnetic fields, from low to high compression factors, and for different upstream temperatures. Although the effect of the magnetic field seems to increase the function $h^* - h_c^*$ in the least cold conditions, its effect is not sufficiently strong to lead to SAE. The apparent contradiction with the ideal gas is resolved if we take into account that γ is a variable function. In weak-shock conditions, the value of γ is high, but ideal gas theory dictates that stability is ensured for any magnetic intensity and any adiabatic index for sufficiently weak shocks. In strong-shock conditions, where ideal gas theory predicted instability for the high γ and low β, the adiabatic index of the compressed material is lowered below $1 + \sqrt{2}$, thereby indicating stability. We refer to the inset in Fig. 7, where the rapid approach of γ_T towards the asymptotic value $5/3 < 1 + \sqrt{2}$ is observed.

IV. SPATIOTEMPORAL EVOLUTION OF THE PERTURBED FLOW

The previous section has been devoted to the specification of the DK stability limits that distinguish the absolutely stable regimes from the neutrally stable regime, the latter being associated with constant-amplitude oscillations of the shock ripples at late time and SAE. The analysis then provides no information on the transient evolution nor on the long-time perturbation amplitudes. To properly describe the effect of the magnetic field intensity in the shocked gas perturbations, which is a problem of great importance in MagLIF schemes, we theoretically calculate the transient evolution of the shock ripple and the postshock variables.

A. Shock ripple amplitude

Since the evolution of the isolated planar shock, either in the DK neutrally stable regime or not, has been extensively studied in previous works [77–79], we do not reproduce the derivations here, but only present the final results. For the decaying-amplitude case $h^* < h_c^*$, the evolution of the shock ripple amplitude is given by

$$\xi_s|_{h \leqslant h_c}(\tau) = \frac{2}{\pi} \int_0^1 \frac{\sqrt{1 - z^2}\sigma_c}{(\sigma_c - \sigma_b z^2)^2 + z^2(1 - z^2)}$$
$$\times \cos\left(z\sqrt{1 - \mathcal{M}_{F2}^2}\,\tau\right) dz, \qquad (39)$$

which involves the parameters

$$\sigma_b = \frac{1 - h^*}{2\mathcal{M}_{F2}}, \tag{40a}$$

$$\sigma_c = \frac{\mathcal{R}\mathcal{M}_{F2}}{1 - \mathcal{M}_{F2}^2} \frac{1 + h^*}{2}. \tag{40b}$$

The asymptotic behavior is $\xi_s(\tau) \sim \tau^{-3/2}$ for $\tau \gg 1$. When $\sigma_b > \sigma_c + 1/(4\sigma_c)$ (or $h^* < h_d^*$), the mathematical expression governing the evolution of the shock ripple remains the same, although the initial exponential damping serves as a clear distinguishing factor for this regime.

When $h^* = h_c^*$, the parameters $\sigma_b = \sigma_c$, and then $\xi_s(\tau) \sim \tau^{-1/2}$. For the case $h^* > h_c^*$ the shock ripple evolution must include the nondecaying contribution, so that

$$\xi_s\big|_{h > h_c}(\tau) = \xi_s\big|_{h \leqslant h_c}(\tau) + \xi_s^\infty \sin\left(\zeta\sqrt{1 - \mathcal{M}_{F2}^2}\,\tau\right), \tag{41}$$

where the normalized frequency is

$$\zeta = \left[\frac{2\sigma_b\sigma_c - 1 - \sqrt{1 + 4\sigma_c(\sigma_c - \sigma_b)}}{2(\sigma_b^2 - 1)}\right]^{1/2}, \tag{42}$$

satisfying $\zeta \geqslant 1$, and the asymptotic amplitude

$$\xi_s^\infty = \frac{\sigma_c}{\zeta^2} \frac{\sigma_c - \sigma_b\zeta^2 + \zeta\sqrt{\zeta^2 - 1}}{\sqrt{1 + 4\sigma_c(\sigma_c - \sigma_b)}}. \tag{43}$$

It can be easily demonstrated that ξ_s^∞ is a monotonic function of h^* bounded by $\xi_s^\infty = 0$ and $\xi_s^\infty = \mathcal{R}/(1 + 2\mathcal{R}\mathcal{M}_{F2} - \mathcal{M}_{F2})$, corresponding to the limits $h^* = h_c^*$ and $h^* = 1 + 2\mathcal{M}_{F2}$, respectively. Note that, for $h^* = h_c^*$, the frequency agrees with the shock fundamental frequency $\zeta = 1$, while it diverges for $h^* = 1 + 2\mathcal{M}_{F2}$.

It is of interest to evaluate these functions in the context of MHD shocks. To simplify the analysis, this section is restricted to the ideal gas EoS, so that the parametric domain is reduced to γ (gas compressibility), β (magnetic field intensity), and $\mathcal{R}$ (shock strength). For example, Fig. 8 shows the temporal evolution of the shock ripple as a function of the dimensionless temporal variable τ. Figure 8(a) is computed for an ideal gas with $\gamma = 1.1$, with density compression ratio $\mathcal{R} = 10$ and two different magnetic field intensities $\beta = 10^{-3}$ (blue curve) and $\beta = 10^3$ (red curve). As expected, the two cases decay in time with the power law $\tau^{-3/2}$ since $h^* < h_c^*$. Given that $\gamma < 2$, the magnetic field exerts a stabilizing effect, promoting the damping of the oscillations. There is an important difference between the two chosen cases, with this γ and R the strong magnetic field causes the case in blue to have $h^* < h_d^*$. These cases are marked in red in Fig. 4(a), where the h_d^* behavior is best seen. Comparing both oscillations, we can see how, although they have the same decay characterizing their asymptotic behavior, the blue curve ($h^* < h_d^*$) undergoes an initial exponential damping. This reduces the order of magnitude of the amplitude substantially in the first oscillations in comparison to the case with $h^* > h_d^*$.

However, Fig. 8(b) shows the case for a high value of the polytropic index $\gamma = 3 > 1 + \sqrt{2}$ for $\mathcal{R} = 1.8$ and the same dimensionless magnetic intensities. In this case, the magnetic field plays an amplifying role, with the case $\beta = 10^{-3}$ (green
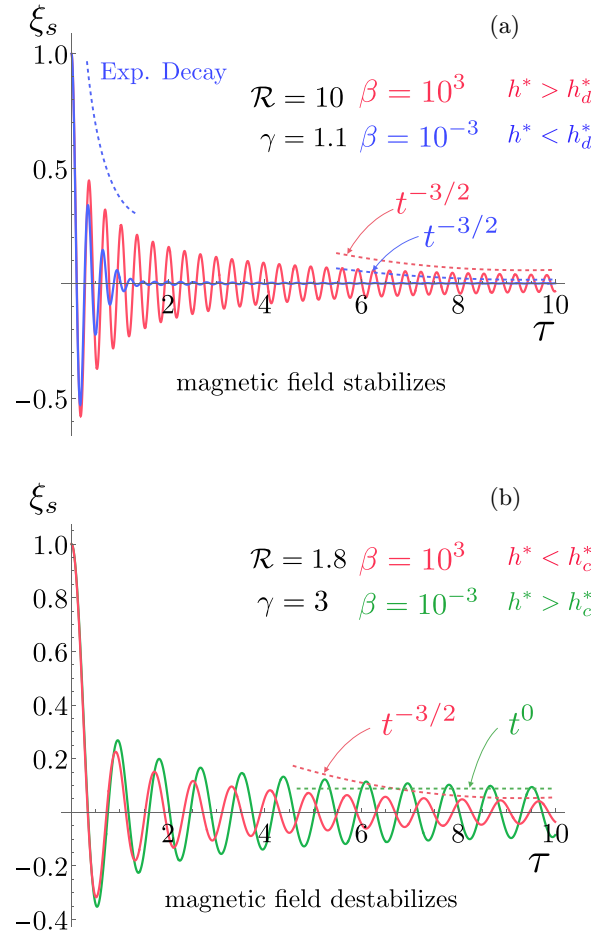

FIG. 8. Long-term shock ripple amplitude for two different gases ($\gamma = 1.1$ and $\gamma = 3$) and shock strengths (for $\mathcal{R} = 10$ and $\mathcal{R} = 1.8$), with the magnetic field being stabilizing (a) and destabilizing (b), respectively. The dimensionless shock position coordinate is $x_s/\lambda = \mathcal{M}_2/(2\pi)\tau$.

curve) displaying a DK neutrally stable shock, and therefore asymptotically approaching a constant nonzero amplitude.

A switch in the stabilizing role of the magnetic field has also been reported for other instabilities of interest for high-energy density systems, such as the ablative Rayleigh-Taylor instability, by García-Rubio *et al.* [80,81]. Returning to Fig. 8, it is found that it takes several wavelengths for the shock to travel to reach the constant-amplitude asymptotic state, where the amplitude of the nondecaying contribution is much larger than the amplitude of the oscillations associated with the decaying counterpart. This characteristic distance will therefore depend on the shock value of ξ_s^∞. Figure 9 shows the asymptotic shock ripple amplitude ξ_s^∞ as a function of $\mathcal{R}$ and β for $\gamma = 3$ (orange-yellow) and $\gamma = 7/2$ (blue-yellow), corresponding to sufficiently high adiabatic indices: $\gamma > 1 + \sqrt{2}$. It is observed a region where ξ_s^∞ is maximum, corresponding to the conditions at which $h^* - h_c^* > 0$ peaks, given in Fig. 3 for an ideal gas. It is also noteworthy that, for the parametric domain considered, which includes relatively high magnetic intensities ($\beta \gtrsim 10^{-3}$), the maximum asymptotic amplitude $\xi_s^\infty \lesssim 10^{-1}$ is one order of magnitude smaller than the initial shock perturbation amplitude.
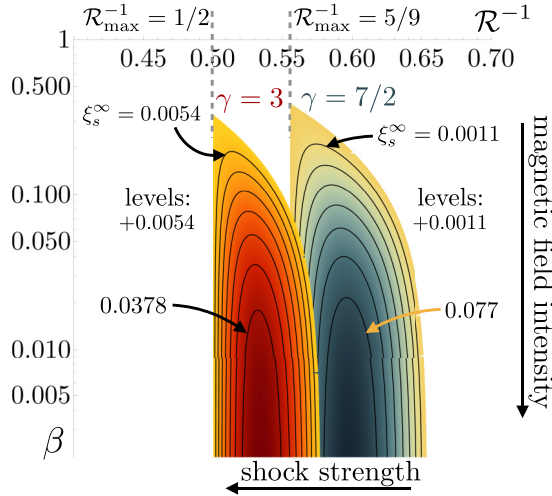
FIG. 9. Isocontours of the asymptotic shock ripple amplitude ξ_s^∞ for the DK neutrally stable conditions associated with highly magnetized shocked ideal gases with $\gamma = 3$ (orange-yellow) and $\gamma = 7/2$ (blue-yellow).

B. Magnetosonic, magnetoentropic, and vortical perturbation field

In the context of the MHD linear waves studied in this problem, Kovasznay's decomposition [82] can effectively segregate downstream perturbations, considering the specific magnetic field orientation that renders no magnetic lines bending. Then the downstream perturbations split into vortical, magnetoentropic, and fast magnetoacoustic modes. In this case, the divergence-free vorticity perturbations generated at the shock are decoupled from the density and magnetic field perturbations. In addition, the alteration in density caused by magnetosonic and entropic perturbations is directly proportional to the perturbations in magnetic field intensity, as represented by the relationship $\delta\rho/\rho_2 = |\delta\vec{B}|/|\vec{B}_2|$. It is important to note that only the latter perturbation corresponds to steady disturbances that would persist in the shocked gas in the absence of dissipation effects.

However, since the change in density associated with the magnetosonic and entropic perturbations is proportional to the perturbations in the magnetic field intensity, where only the latter correspond to steady disturbances that would remain in the shocked gas in the absence of dissipation effects. In what follows, the amplitude of the steady perturbations is analyzed. In what concerns the fast magnetosonic mode, the perturbations induced by the shock ripple dynamics are

$$\bar{p}^*(\bar{x} \gg 1) = \bar{p}_F^* \cos(k_F\bar{x} - \omega_F\tau), \tag{44}$$

where the dispersion relationship of the fast magnetosonic wave equation $\omega_F^2 = k_F^2 + 1$ and the compatibility condition at the shock $\zeta\sqrt{1 - \mathcal{M}_{F2}^2} = (\omega_F - \mathcal{M}_{F2}k_F)$ allow us to write

$$k_F = \frac{\zeta\mathcal{M}_{F2} - \sqrt{\zeta^2 - 1}}{\sqrt{1 - \mathcal{M}_{F2}^2}}, \tag{45a}$$

$$\omega_F = \frac{\zeta - \mathcal{M}_{F2}\sqrt{\zeta^2 - 1}}{\sqrt{1 - \mathcal{M}_{F2}^2}}, \tag{45b}$$

that correspond to the longitudinal wave number and frequency in the shocked gas reference frame. The asymptotic magnetosonic amplitude is readily given by the linearized RH equation (14a):

$$\bar{p}_F^* = \frac{\sigma_d}{\zeta} \frac{\sigma_b\zeta^2 - \sigma_c - \zeta\sqrt{\zeta^2 - 1}}{\sqrt{1 + 4\sigma_c(\sigma_c - \sigma_b)}}, \tag{46}$$

where σ_d is defined as

$$\sigma_d = -\frac{\mathcal{M}_{F2}^2(\mathcal{R} - 1)}{\sqrt{1 - \mathcal{M}_{F2}^2}} \tag{47}$$

for conciseness.

Akin to the previous asymptotic expression for the shock ripple ξ_s^∞, the asymptotic shock pressure amplitude in Eq. (46) is zero when $h^* = h_c^*$, yet it grows unbounded as $h^* \to 1 + 2\mathcal{M}_{F2}$. The propagating fast magnetosonic waves involve changes in the velocity perturbations. In particular, they correspond to potential flow disturbances that can be derived with the aid of Eq. (9) by imposing $\nabla \times \delta\vec{v}_F = 0$. However, it is simpler to withdraw the acoustic velocity perturbations (both longitudinal and transverse components) from the Euler momentum conservation equations to yield

$$\bar{u}_F^*(\bar{x} \gg 1) = \frac{k_F}{\omega_F}\bar{p}_F^*\cos(k_F\bar{x} - \omega_F\tau), \tag{48a}$$

$$\bar{v}_F^*(\bar{x} \gg 1) = \frac{1}{\omega_F}\bar{p}_F^*\sin(k_F\bar{x} - \omega_F\tau). \tag{48b}$$

The postshock perturbation variables of interest also include the vorticity and the magnetoentropic field, since they remain frozen to the fluid particles in the absence of dissipation effects. For example, the steady-rotational perturbations, which are isobaric in the linear limit, are governed by

$$\frac{\partial^2\bar{u}_r}{\partial\bar{x}^2} - \bar{u}_r = \Omega, \tag{49a}$$

$$\frac{\partial^2\bar{v}_r}{\partial\bar{x}^2} - \bar{v}_r = -\frac{\partial\Omega}{\partial\bar{x}}, \tag{49b}$$

where the function

$$\begin{aligned}\Omega(\bar{x} \gg 1) &= \frac{\partial\bar{v}_r}{\partial\bar{x}} + \bar{u}_r \\ &= \frac{(1 + h^*)(\mathcal{R} - 1)}{2\mathcal{M}_{F2}}\bar{p}_F^*\sin\left(\sqrt{\mathcal{M}_{F2}^{-2} - 1}\,\zeta\,\bar{x}\right)\end{aligned} \tag{50}$$

represents the dimensionless vorticity field. When dissipation effects are not present, and the Alfven mode is absent, the generation of vorticity-entropy perturbations in the shocked gas is exclusively confined to the distorted shock front. Along with the vorticity perturbations, the oscillating shock generates density-entropic perturbations that are not related to the fast magnetosonic disturbances. These steady disturbances come along with a change in the magnetic field, so that the postshock gas leaves behind a modulated magnetodensity field in the form

$$\bar{\rho}_e(\bar{x} \gg 1) = \frac{-h^*(l + 1) + \mathcal{M}_{F2}^2}{h^*l + \mathcal{M}_{F2}^2}\bar{p}_F^*\cos\left(\sqrt{\mathcal{M}_{F2}^{-2} - 1}\,\zeta\,\bar{x}\right), \tag{51}$$

with the auxiliary parameter l defined as

$$l = \frac{2\mathcal{R}\mathcal{M}_{F2}^2}{\mathcal{M}_{F1}^2(2+\beta\gamma)} \quad (52)$$

for conciseness. The density field is composed by the sum of the acoustic and entropic modes. The acoustic component is equal to the pressure component through Eq. (7c), and the entropic one is imprinted in space with the equally perturbed magnetic field.

V. NUMERICAL SIMULATIONS

To study a numerical application of the DK instability we utilize the FLASH code [83,84]. FLASH is a publicly available, high-performance computing, multiphysics, adaptive mesh refinement (AMR), finite-volume (FV) Eulerian hydrodynamics, and magnetohydrodynamics (MHD) code, developed at the University of Rochester by the Flash Center for Computational Science [63]. The code scales well to over 100 000 processors and uses a variety of parallelization techniques to optimally utilize hardware resources. FLASH's modularity provides users with a significant degree of flexibility and control that enables the modeling of problems in a wide range of disciplines, including fluid dynamics, hydrodynamic and MHD turbulence, astrophysics, cosmology, combustion, fusion, and high-energy density physics (HEDP). Over the past decade, FLASH has been augmented with extensive HEDP and extended-MHD capabilities [84] as part of the U.S. DOE NNSA-funded FLASH HEDP Initiative and through direct support by the Los Alamos National Laboratory (LANL), the Lawrence Livermore National Laboratory (LLNL), and the Laboratory for Laser Energetics (LLE). These include multiple state-of-the-art hydrodynamic and MHD shock-capturing solvers [85]; three-temperature extensions with anisotropic thermal conduction, heat exchange, multigroup radiation diffusion, tabulated multimaterial equations of state and opacities, laser energy deposition, and numerous simulated diagnostics [84,86]. The FLASH code and its capabilities have been verified through extensive benchmarks and code-to-code comparisons and have been validated through direct application to scores of laser-driven and pulsed power-driven laboratory experiments, in premier facilities around the world.

The nature of the DK instability discussed in this article presents several difficulties for its predictability through numerical simulations. Shocks, which are fronts without thickness, can cause significant changes in flow variables by several orders of magnitude. Small-amplitude perturbations occurring at the shock front, which do not grow in the neutral stability/SAE regime, are challenging to accurately capture and track over time using numerical simulations. FLASH includes multiple state-of-the-art hydrodynamic and MHD shock capture schemes, among which the HLL solver (Harten, Lax, and van Leer [87]) was found to be the best option for this study. FLASH's other, more accurate, solvers generated noise that was comparable in magnitude to the disturbances being studied. HLL-type solvers, however, are a class of more diffusive approximate Riemann solvers that possess high levels of robustness [88,89]. These solvers have an essential feature that makes them particularly suitable for handling small
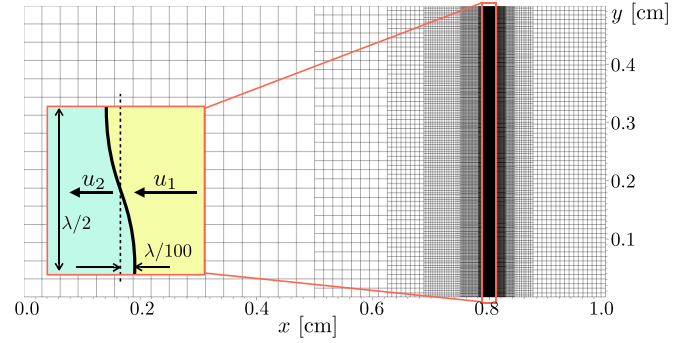

FIG. 10. Sketch of the numerical setup that includes the domain limits and the perturbation wavelength and amplitude

amplitude perturbations at shock fronts: They do not require the use of added artificial viscosity, which could dampen the oscillations that are being investigated. The simulations used in this study employ a nonuniform square-box mesh, where the size of the cells at the front is 1.625×10^{-4} cm. The mesh is used to compute a shock that is initially distorted with a half-wavelength of 0.5 cm and an amplitude of 0.01 cm. Additionally, an AMR approach is employed to evaluate any displacement of the shock front as the amplitude decreases, if required.

The computational domain is depicted in Fig. 10. The simulation begins with an initial solution that is prescribed by the Rankine-Hugoniot equations for a fast MHD shock. The inlet and outlet boundary conditions are designed to maintain the average shock position static and are consistent with each other. Symmetric boundary conditions define the upper and lower limits of the domain, while outflow (zero gradient) boundary conditions are used for the inlet and outlet limits. These boundary conditions are a suitable approximation to nonreflective conditions, provided that a sufficiently large downstream domain is defined, as per the isolated-shock boundary condition specified in the linear analysis. Since shock perturbations do not affect the upstream flow, the corresponding domain ahead of the shock is reduced to optimize computational efficiency.

The evolution of the shock ripple amplitude is shown in Fig. 11(a) for a fast MHD shock in an ideal gas, with adiabatic index $\gamma = 1.2$, mass-compression ratio $\mathcal{R} = 6$ and two distinguished cases: low-magnetized ($\beta = 10^3$) and high-magnetized ($\beta = 10^{-3}$) gas flow. The former, plotted in red, corresponds to a regular decaying solution ($h_d^* < h^* < h_c^*$); while the latter, in blue, corresponds to an initially exponentially damped regime ($-1 < h^* < h_d^*$). The plot also displays both the theoretical solution given by Eq. (39), plotted as a solid line, and the numerical solution with FLASH (empty circles). Figure 11(b) also provides the evolution of the shock ripple amplitude, but this case is computed for $\gamma = 4$ and $\mathcal{R} = 1.5594$ with the same magnetic field intensities as in Fig. 11(a): $\beta = 10^3$ and $\beta = 10^{-3}$. The former, plotted in red, corresponds to a regular decaying solution ($h^* < h_c^*$); while the latter, in green, corresponds to a long-time nondecaying condition ($h^* > h_c^*$), whose theoretical solution is given by Eq. (41). Stable low magnetized solutions have been calculated in FLASH with zero magnetic field, but they are very
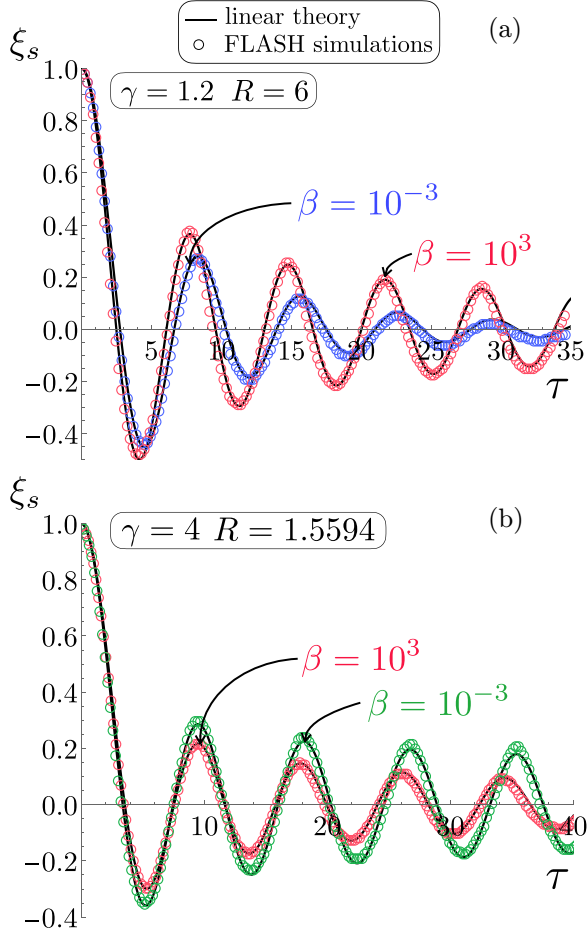
FIG. 11. Evolution of the shock ripple amplitude for very low ($\beta = 10^3$) and very high ($\beta = 10^{-3}$) magnetic field intensities in an ideal gas EoS. (a) $\gamma = 1.2$ and $\mathcal{R} = 6$; (b) $\gamma = 4$ and $\mathcal{R} = 1.5594$. Solid black lines correspond to linear-theory results and empty circles to FLASH computations.

close to $\beta = 10^3$. Both comparisons shown in Fig. 11 are detailed for better understanding in Fig. 4 (orange), and make use of the same color code as in Fig. 8.

Along with the shock-corrugation evolution, it is of interest to numerically investigate the postshock perturbation flow. With this motivation, Fig. 12 displays the pressure and density fields associated with the case $h^* > h_c^*$ in Fig. 11(a), orange curve: $\gamma = 4$, $\mathcal{R} = 1.5594$, and $\beta = 10^{-3}$. The color scheme is deliberately saturated to better highlight the disturbed field. It is readily noted that pressure and density exhibit two different spatial frequencies. In the case of the pressure field, the only source of perturbations corresponds to the traveling magnetosonic waves that are radiated downstream from the shock. The wavelength of these waves can be determined directly from Eq. (45), which predicts a wavelength of 0.59 cm. This value is in good agreement with the results of the simulation. As per the density field, the numerical solution displays both acoustic plus entropic contributions simultaneously. However, since the theoretical prediction for the entropic wave number is $\sqrt{M_{F2}^{-2} - 1} \times \zeta$, giving 0.48 cm for the simulation conditions, we can conclude that the acoustic contribution is relatively weak. Besides, while the numerical simulations exhibit a perfectly sinusoidal downstream lobular pattern, as predicted by the theoretical analysis, the characteristic lengths are accurately reproduced.

To further assess the accuracy of the simulations or the validity of the theoretical model, we will now turn our attention to the amplitude of the perturbations. By simple inspection of the color scale, we find that $\delta p/p_2 \sim 2.4 \times 10^{-2}$ and $\delta\rho/\rho_2 \sim 9.6 \times 10^{-3}$. These values can be used to calculate the amplitude of the total pressure field perturbation (thermal plus magnetic contributions) with use made of the expression

$$\bar{p}_{\text{num}}^* = \frac{1}{\varepsilon}\left[\frac{\delta p_2}{p_2} + \frac{2\mathcal{R}_s^2}{\mathcal{P}_s\beta}\frac{\delta B_2}{B_2}\right]\frac{\mathcal{P}_s\mathcal{R}_s\mathcal{M}_{F2}^2}{\mathcal{M}_{F1}^2(\gamma + 2/\beta)}, \tag{53}$$

which yields $\bar{p}_{\text{num}}^* = 0.0614$ for the conditions simulated in Fig. 12. The theoretical prediction for the asymptotic value of the pressure perturbation amplitudes (the lowest value reached in the long-time regime) is $\bar{p}_\infty^* = 0.0547$, which is only slightly lower than the value observed in the simulations. This is consistent with the fact that the downstream magnetosonic perturbations decay as the amplitude of the shock ripple oscillations decreases, as shown in Fig. 11. It should be
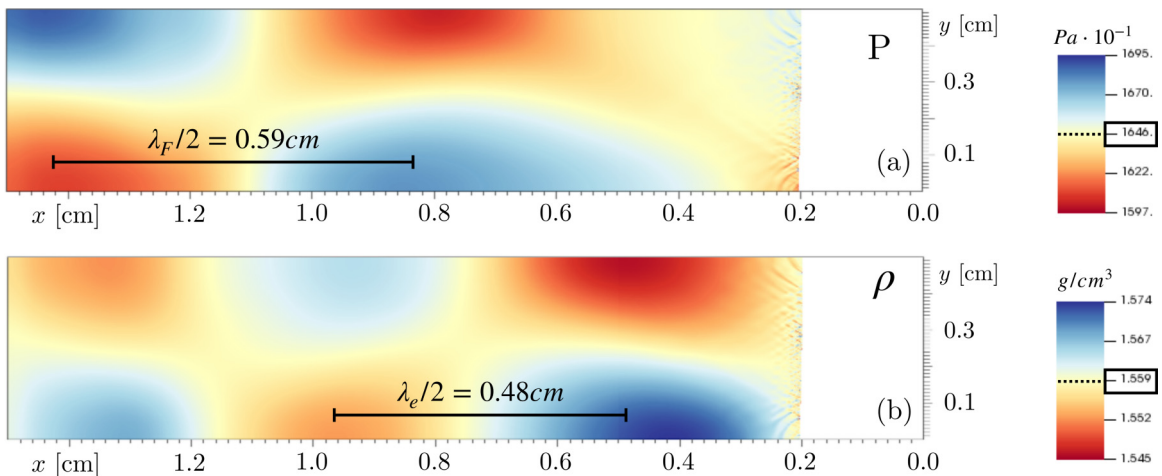

FIG. 12. Downstream pressure (a) and density (b) fields for $t = 1.32 \times 10^{-2}$ s ($\tau = 7.11$), and annotations for comparison with the analytical downstream wavelength, in an ideal gas $\gamma = 4$ with a mass-compression ratio $\mathcal{R} = 1.5594$ and a magnetic field of $\beta = 10^{-3}$

noted that this statement applies to isolated-shock conditions, as the inclusion of a supporting mechanism would increase the amplitude of the downstream pressure perturbations compared to those generated at the shock [53].

VI. CONCLUSIONS

We have presented a linear theoretical analysis of the stability of fast magnetosonic shocks whose perturbation field plane is perpendicular to the magnetic field lines. In this setup, the mathematical description is similar to that used in a gas-dynamics problem, with the total pressure (magnetic plus thermal) playing the role of the thermal pressure field, and the fast magnetosonic speed being equivalent to the acoustic sound speed in the gas-dynamics problem. Therefore, by applying the convenient definitions, the stability limits in terms of the classic DK parameter h (here conveniently redefined as h^*) agree with those associated with conventional shocks and initially presented in Refs. [40,41].

A theoretical model has been developed for any type of equation of state (EoS) and then applied to three different cases, namely ideal gases, van der Waals gases, and condensed materials related to simple metals (specifically aluminium in this case) through a three-term EoS. In addition, numerical simulations have been conducted using the FLASH code for ideal gases. The agreement between the theoretical model and the numerical simulations is excellent, as can be seen from the comparison of the oscillation frequencies and the prediction of the transient evolution of the shock-ripple behavior. The main conclusions drawn from this study are listed in the following.

(i) For an ideal gas EoS, when $\gamma < 2$, the effect of the magnetic field is to decrease the amplitude of the shock ripple oscillations, with the possibility of exerting an initially exponential damping for sufficiently strong magnetic fields $h^* < h_d^*$. The effect of the magnetic field reverses for $\gamma > 2$. Moreover, when the adiabatic index $\gamma > 1 + \sqrt{2}$, the shock can enter the DK neutrally stable regime $h^* > h_c^*$, or SAE, if the magnetic field intensity is sufficiently large and the shock is sufficiently strong. Weak shocks are found to be always stable regardless of the adiabatic index and the magnetic intensity ($h^* < h_c^*$).

(ii) The stability conditions for a van der Waals EoS are affected by additional factors related to intermolecular attraction and covolume. In addition to the magnetic-induced neutral stability/SAE observed in ideal gases for strong shocks and high adiabatic indices, a purely acoustic instability exists for weak magnetic fields and low values of γ. This is equivalent to that found by Bates and Montgomery [61] and later on studied in similar shock configurations [52,60].

(iii) We have found that for a three-term EoS describing aluminium, the shock remains stable over the whole range of parameters explored. Although neutral stability/SAE has been predicted for strong shocks in low-compressible, highly magnetized media [see point (i) for ideal gases], the compression of the shock causes a reduction in the adiabatic index that keeps it below the instability threshold of $1 + \sqrt{2}$. We suggest that additional examples with different metals could be studied to further explore this phenomenon.

Several future works are planned to extend the current study. One of them is to examine the effect of magnetic fields oriented in a direction other than perpendicular to the perturbation field. This orientation will introduce additional modes downstream, namely the Alfvén and slow magnetosonic modes. Another future work aims to enhance the analysis by utilizing more realistic boundary conditions that accurately represent high-energy-density experiments. In addition, nonlinear perturbations will be explored using FLASH simulations in this study.

Another essential extension of the present work involving FLASH is its generalization for convergent cylindrical geometry appropriate for ICF and HEDP applications, including MagLIF and SZP. We cannot simply modify the analytical stability study [90] of the baseline Guderley's converging-shock self-similar solution [91] because such solutions do not exist with nonideal EoS permitting the DK instability; cf. the discussion in Refs. [60,92–94] and references therein. We will have to do the stability analysis numerically, the present work serving as the necessary step of the FLASH code verification for modeling the evolution of small-amplitude shock-front perturbations.

APPENDIX: EOS FOR SIMPLE METALS

To describe the shock compression in condensed materials, the three-term EoS is employed. The model, which corresponds to that described in Chapter XI, Sec. 6, of Ref. [95] and used as an example in Refs. [60,96], provides a reasonably accurate description in the pressure range up to several Mbar. The pressure and the specific internal energy are presented as sums of three well-defined contributions,

$$p(\rho, T) = p_c(\rho) + p_l(\rho, T) + p_e(\rho, T), \qquad \text{(A1)}$$

$$E(\rho, T) = E_c(\rho) + E_l(T) + E_e(\rho, T), \qquad \text{(A2)}$$

where the cold or elastic terms p_c and E_c are related to the interaction forces between the atoms of the material at $T = 0$ and therefore they depend only on the material density ρ. The thermal ion (lattice) terms p_l and E_l as well as the thermal

electron terms p_e and E_e are functions of both density and temperature.

For the cold metal, we use Molodets' analytical approximation [73] for the density dependence of the Grüneisen coefficient

$$\Gamma = \frac{2}{3} + \frac{2\rho_{0m}}{m\rho - \rho_{0m}}, \tag{A3}$$

where ρ_{0m} is the density extrapolated to zero temperature and pressure and m is a dimensionless constitutive parameter.

With the aid of the Landau–Slater formula [97,98] and the definition of cold energy $p_c = \rho^2 dE_c/d\rho$,

$$p_c(z) = \frac{3K_{0m}}{(m-1)^4}\left(\frac{1}{5}m^4 z^{5/3} - 2m^3 z^{2/3} - 6m^2 z^{-1/3}\right.$$
$$\left. + mz^{-4/3} - \frac{1}{7}z^{-7/3} - \frac{1}{5}m^4 + 2m^3 + 6m^2 - m + \frac{1}{7}\right), \tag{A4}$$

$$E_c(z) = \frac{3K_{0m}}{\rho_{0m}(m-1)^4}\left(\frac{3}{10}m^4 z^{2/3} - 6m^3 z^{-1/3}\right.$$
$$+ \frac{7m^4 - 70m^3 - 210m^2 + 35m - 5}{35}z^{-1} + \frac{9}{2}m^2 z^{-4/3}$$
$$- \frac{3}{7}mz^{-7/3} + \frac{3}{70}z^{-10/3}$$
$$\left. - \frac{35m^4 + 280m^3 - 105m^2 + 40m - 7}{70}\right), \tag{A5}$$

where K_{0m} is the adiabatic bulk modulus extrapolated to zero temperature and pressure and $z = \rho/\rho_{0m}$ is the normalized density. For the ion lattice (thermal) contributions to the pressure and internal energy are

$$p_l(z, T) = \rho_{0m}\frac{3}{m_a}z\Gamma(z)k_B T, \tag{A6}$$

$$E_l(T) = \frac{3}{m_a}k_B T, \tag{A7}$$

where m_a is the atomic mass and k_B is the Boltzmann constant. The electron contributions are

$$p_e(z, T) = \frac{1}{3}\beta_0 z^{1/3}T^2, \tag{A8}$$

$$E_e(z, T) = \frac{1}{2}\beta_0 z^{-2/3}T^2, \tag{A9}$$

where β_0 is determined by the number of free electrons per unit mass of the material at $T = 0$ and $\rho = \rho_{0m}$. In deriving Eq. (A9), if the electronic Grüneisen coefficient is taken to be 2/3, then the density and temperature dependence would correspond exactly to a free electron gas at a temperature well below the Fermi energy.

The formulation calls for the definition of the speed of sound which takes the form

$$c^2 = \frac{\gamma_c p_c + \gamma_l p_l + \gamma_e p_e}{p_c + p_l + p_e}\frac{p}{\rho}, \tag{A10}$$

where the term accompanying the factor p/ρ is the mean effective value of the adiabatic index. The corresponding values of γ_c, γ_l, and γ_e associated with the cold, lattice, and electronic contributions are, respectively,

$$\gamma_c = \frac{K_{0m}}{p_c}\frac{(mz-1)^4}{(m-1)^4 z^{10/3}}, \tag{A11a}$$

$$\gamma_l = \frac{d\ln\Gamma}{d\ln z} + \Gamma + 1, \tag{A11b}$$

$$\gamma_e = \frac{5}{3}. \tag{A11c}$$

---

[1] H. Abu-Shawareb, R. Acree, P. Adams, J. Adams, B. Addis, R. Aden, P. Adrian, B. B. Afeyan, M. Aggleton, L. Aghaian *et al.*, Phys. Rev. Lett. **129**, 075001 (2022).

[2] R. Betti, A milestone in fusion research is reached, Nat. Rev. Phys. **5**, 6 (2023).

[3] I. R. Lindemuth and R. C. Kirkpatrick, Nucl. Fusion **23**, 263 (1983).

[4] I. R. Lindemuth and R. C. Kirkpatrick, Fusion Technol. **20**, 829 (1991).

[5] R. C. Kirkpatrick, I. R. Lindemuth, and M. S. Ward, Fusion Technol. **27**, 201 (1995).

[6] I. R. Lindemuth and R. E. Siemon, in *Proceeding of the AIP Conference*, AIP Conf. Proc. No. 1154 (American Institute of Physics, College Park, MD, 2009), pp. 68–69.

[7] S. F. Garanin and R. E. Reinovsky, Report No. LA-UR-13-29094, Los Alamos National Lab. (LANL), Los Alamos, 2015, see https://www.osti.gov/biblio/1178554.

[8] I. R. Lindemuth, Phys. Plasmas **22**, 122712 (2015).

[9] I. R. Lindemuth, Phys. Plasmas **24**, 055602 (2017).

[10] J. G. Linhart, H. Knoepfel, and C. Gourian, Nucl. Fusion, Suppl. (1962).

[11] S. A. Slutz, M. C. Herrmann, R. A. Vesey, A. B. Sefkow, D. B. Sinars, D. C. Rovang, K. J. Peterson, and M. E. Cuneo, Phys. Plasmas **17**, 056303 (2010).

[12] S. A. Slutz and R. A. Vesey, Phys. Rev. Lett. **108**, 025003 (2012).

[13] S. A. Slutz, W. A. Stygar, M. R. Gomez, K. J. Peterson, A. B. Sefkow, D. B. Sinars, R. A. Vesey, E. M. Campbell, and R. Betti, Phys. Plasmas **23**, 022702 (2016).

[14] P. F. Schmit and D. E. Ruiz, Phys. Plasmas **27**, 062707 (2020).

[15] D. A. Yager-Elorriaga, M. R. Gomez, D. E. Ruiz, S. A. Slutz, A. J. Harvey-Thompson, C. A. Jennings, P. F. Knapp, P. F. Schmit, M. R. Weis, T. J. Awe *et al.*, Nucl. Fusion **62**, 042015 (2022).

[16] H. U. Rahman, F. J. Wessel, and N. Rostoker, Phys. Rev. Lett. **74**, 714 (1995).

[17] H. U. Rahman, P. Ney, N. Rostoker, and F. J. Wessel, Astrophys. Space Sci. **323**, 51 (2009).

[18] F. J. Wessel, P. Ney, R. Presura *et al.*, IEEE Trans. Plasma Sci. **43**, 2463 (2015).

[19] F. J. Wessel, H. U. Rahman, P. Ney, J. Valenzuela, F. Beg, E. McKee, and T. Darling, in *Proceedings of the AIP*

Conference, AIP Conf. Proc. No. 1721 (AIP Publishing LLC, Melville, NY, 2016), p. 060002.

[20] H. U. Rahman, E. Ruskov, P. Ney, F. Conti, J. C. Valenzuela, N. Aybar, J. Narkis, F. N. Beg, E. Dutra, and A. Covington, Phys. Plasmas **26**, 052706 (2019).

[21] E. Ruskov, P. Ney, and H. U. Rahman, Phys. Plasmas **27**, 042709 (2020).

[22] E. Ruskov, P. Ney, and H. U. Rahman, Phys. Plasmas **28**, 112701 (2021).

[23] I. R. Lindemuth, M. R. Weis, and W. L. Atchison, Phys. Plasmas **25**, 102707 (2018).

[24] I. R. Lindemuth, Phys. Plasmas **28**, 014701 (2021).

[25] E. Ruskov, P. Ney, and H. U. Rahman, Phys. Plasmas **28**, 014702 (2021).

[26] I. R. Lindemuth, Phys. Plasmas **29**, 084702 (2022).

[27] E. Ruskov, P. Ney, and H. U. Rahman, Phys. Plasmas **29**, 084703 (2022).

[28] R. D. Jones and W. C. Mead, Nucl. Fusion **26**, 127 (1986).

[29] L. J. Perkins, D.-M. Ho, B. G. Logan, G. B. Zimmerman, M. A. Rhodes, D. J. Strozzi, D. T. Blackfield, and S. A. Hawkins, Phys. Plasmas **24**, 062708 (2017).

[30] J. D. Moody, B. Pollock, H. Sio, D. J. Strozzi, D.-M. Ho, C. A. Walsh, G. E. Kemp, B. Lahmann, S. O. Kucheyev, B. Kozioziemski *et al.*, Phys. Rev. Lett. **129**, 195002 (2022).

[31] C. A. Walsh, S. O'Neill, J. P. Chittenden, A. J. Crilly, B. Appelbe, D. J. Strozzi, D. Ho, H. Sio, B. Pollock, L. Divol *et al.*, Phys. Plasmas **29**, 042701 (2022).

[32] G. Zimmerman, D. Ho, A. L. Velikovich, and J. Moody, Magnetized ICF for high yield, reduction of laser energy, and the generalization of the GLP with B field, in *64th Annual Meeting of the APS Division of Plasma Physics MondayFriday, October 1721, 2022; Spokane, Washington* (Bulletin of the American Physical Society, 2022).

[33] J. Lindl, *Inertial Confinement Fusion: The Quest for Ignition and Energy Gain Using Indirect Drive* (American Institute of Physics, College Park, MD, 1998).

[34] R. S. Craxton, K. S. Anderson, T. R. Boehly, V. N. Goncharov, D. R. Harding, J. P. Knauer, R. L. McCrory, P. W. McKenty, D. D. Meyerhofer, J. F. Myatt *et al.*, Phys. Plasmas **22**, 110501 (2015).

[35] Y. Zhou, Rayleigh–Taylor and Richtmyer–Meshkov instability induced flow, turbulence, and mixing. I, Phys. Rep. **720**, 1 (2017).

[36] Y. Zhou, Rayleigh–Taylor and Richtmyer–Meshkov instability induced flow, turbulence, and mixing. II, Phys. Rep. **723**, 1 (2017).

[37] Y. Zhou, T. T. Clark, D. S. Clark, S. Gail Glendinning, M. Aaron Skinner, C. M. Huntington, O. A. Hurricane, A. M. Dimits, and B. A. Remington, Turbulent mixing and transition criteria of flows induced by hydrodynamic instabilities, Phys. Plasmas **26**, 80901 (2019).

[38] Y. Zhou, R. J. Williams, P. Ramaprabhu, M. Groom, B. Thornber, A. Hillier, W. Mostert, B. Rollin, S. Balachandar, P. D. Powell *et al.*, Physica D **423**, 132838 (2021).

[39] A. E. Roberts, *See National Technical Information Service Document PB2004-100597 [A. E. Roberts, Los Alamos Scientific Laboratory Report No. LA-299 1945 (unpublished)]* (National Technical Information Service, Springfield, VA, 1945).

[40] S. P. D'yakov, Shock wave stability, Zh. Eksp. Teor. Fiz **27**, 288 (1954).

[41] V. M. Kontorovich, On the shock waves stability, Zh. Eksp. Teor. Fiz **33**, 1525 (1957).

[42] L. D. Landau and E. M. Lifshitz, *Fluid Mechanics*, 2nd ed. (Pergamon Press, Oxford/New York, 1987).

[43] P. Clavin and G. Searby, *Combustion Waves and Fronts in Flows: Flames, Shocks, Detonations, Ablation Fronts, and Explosion of Stars* (Cambridge University Press, Cambridge, UK, 2016).

[44] V. Fortov, *Intense Shock Waves on Earth and in Space* (Springer International Publishing, Berlin, 2021).

[45] N. C. Freeman, A theory of the stability of plane shock waves, Proc. R. Soc. Lond. A Math. Phys. Sci. **228**, 341 (1955).

[46] P. M. Zaidel', J. Appl. Math. Mech. **24**, 316 (1960).

[47] I. M. Nikolaev, J. Appl. Math. Mech. **29**, 785 (1965).

[48] J. W. Bates, J. Fluid Mech. **691**, 146 (2012).

[49] R. Menikoff and B. J. Plohr, Rev. Mod. Phys. **61**, 75 (1989).

[50] N. M. Kuznetsov, Sov. Phys. Usp. **32**, 993 (1989).

[51] A. V. Konyukhov, P. R. Levashov, and A. P. Likhachev, J. Phys.: Conf. Ser. **1556**, 012022 (2020).

[52] J. G. Wouchuk and J. L. Cavada, Phys. Rev. E **70**, 046303 (2004).

[53] A. Calvo-Rivera, A. L. Velikovich, and C. Huete, J. Fluid Mech. **964**, A33 (2023).

[54] C. S. Gardner and M. D. Kruskal, Phys. Fluids **7**, 700 (1964).

[55] J. J. Erpenbeck, Phys. Fluids **5**, 1181 (1962).

[56] Y. Trakhinin, Commun. Math. Phys. **236**, 65 (2003).

[57] I. M. Rutkevich and M. Mond, J. Plasma Phys. **48**, 345 (1992).

[58] M. Dieckmann, C. Huete, F. Cobos, A. Bret, D. Folini, B. Eliasson, and R. Walder, PIC simulations of stable surface waves on a subcritical fast magnetosonic shock front, Phys. Scr. **98**, 095603 (2023).

[59] L. D. Landau and E. M. Lifshitz, *Electrodynamics of Continuous Media*, Vol. 8 (Pergamon Press, Oxford, UK, 1960).

[60] C. Huete, A. L. Velikovich, D. Martínez-Ruiz, and A. Calvo-Rivera, J. Fluid Mech. **927**, A35 (2021).

[61] J. W. Bates and D. C. Montgomery, Phys. Rev. Lett. **84**, 1180 (2000).

[62] P. Tzeferacos, M. Fatenejad, N. Flocke, G. Gregori, D. Q. Lamb, D. Lee, J. Meinecke, A. Scopatz, and K. Weide, High Energy Density Phys. **8**, 322 (2012).

[63] http://FLASH.rochester.edu.

[64] S. A. Kaplan and K. P. Stanyukovich, The solution of magneto-gas dynamic equations for one-dimensional motion, Doklady Akad. Nauk SSSR **95**, 769 (1954).

[65] S. Segre, Nuovo Cim. **9**, 1054 (1958).

[66] J. W. Bates, Phys. Rev. E **69**, 056313 (2004).

[67] P. Clavin and B. Denet, J. Fluid Mech. **897**, A30 (2020).

[68] D. Ryu and E. T. Vishniac, Astrophys. J. **313**, 820 (1987).

[69] J. Grun, J. Stamper, C. Manka, J. Resnick, R. Burris, J. Crawford, and B. H. Ripin, Phys. Rev. Lett. **66**, 2738 (1991).

[70] R. Ishizaki and K. Nishihara, Phys. Rev. Lett. **78**, 1920 (1997).

[71] C. Hunter, J. Fluid Mech. **8**, 241 (1960).

[72] A. Calvo-Rivera, C. Huete, and A. Velikovich, Phys. Fluids **34**, 046106 (2022).

[73] A. M. Molodets, Cambust. Explos. Shock Waves **31**, 620 (1995).

[74] S. B. Kormer, A. I. Funtikov, V. D. Urlin, and A. N. Kolesnikova, Dynamic compression of porous metals and the equation of state with variable specific heat at high temperatures, J. Exptl. Theoret. Phys. (U.S.S.R.) **42**, 686 (1962) [Sov. Phys. JETP **15**, 477 (1962)].

[75] L. L. Altgilbers, I. Grishnaev, I. R. Smith, Y. Tkach, M. D. Brown, B. M. Novac, I. Tkach *et al.*, *Magnetocumulative Generators* (Springer, Berlin, 2000).

[76] G. A. Shneerson, M. I. Dolotenko, and S. I. Krivosheev, *Strong and Superstrong Pulsed Magnetic Fields Generation*, Vol. 9 (Walter de Gruyter GmbH & Co KG, 2014).

[77] F. C. Campos and J. G. Wouchuk, Phys. Rev. E **90**, 053007 (2014).

[78] C. Huete and M. Vera, J. Fluid Mech. **879**, 54 (2019).

[79] C. Huete, F. Cobos-Campos, E. Abdikamalov, and S. Bouquet, Phys. Rev. Fluids **5**, 113403 (2020).

[80] F. García-Rubio, R. Betti, J. Sanz, and H. Aluie, Phys. Plasmas **28**, 012103 (2021).

[81] F. García-Rubio, R. Betti, J. Sanz, and H. Aluie, Phys. Plasmas **27**, 112715 (2020).

[82] L. S. Kovasznay, J. Aeronaut. Sci. **20**, 657 (1953).

[83] B. Fryxell, K. Olson, P. Ricker, F. X. Timmes, M. Zingale, D. Q. Lamb, P. MacNeice, R. Rosner, J. W. Truran, and H. Tufo, Astrophys. J. Suppl. Ser. **131**, 273 (2000).

[84] P. Tzeferacos, M. Fatenejad, N. Flocke, C. Graziani, G. Gregori, D. Q. Lamb, D. Lee, J. Meinecke, A. Scopatz, and K. Weide, FLASH MHD simulations of experiments that study shock-generated magnetic fields, High Energy Density Physics **17**, 24 (2015).

[85] D. Lee, J. Comput. Phys. **243**, 269 (2013).

[86] P. Tzeferacos, A. Rigby, A. Bott, A. R. Bell, R. Bingham, A. Casner, F. Cattaneo, E. M. Churazov, J. Emig, N. Flocke *et al.*, Phys. Plasmas **24**, 041404 (2017).

[87] B. Einfeldt, C.-D. Munz, P. L. Roe, and B. Sjögreen, J. Comput. Phys. **92**, 273 (1991).

[88] E. F. Toro, in *Riemann Solvers and Numerical Methods for Fluid Dynamics* (Springer, Berlin, 2009), pp. 315–344.

[89] K. Murawski and D. Lee, Numerical methods of solving equations of hydrodynamics from perspectives of the code FLASH, Bull. Pol. Acad. Sci.: Tech. Sci. **59**, 81 (2011).

[90] M. Murakami, J. Sanz, and Y. Iwamoto, Phys. Plasmas **22**, 072703 (2015).

[91] G. Guderley, Starke kugelige und zylindrische verdichtungsstosse in der nahe des kugelmitterpunktes bnw. der zylinderachse, Luftfahrtforschung **19**, 302 (1942).

[92] L. I. Sedov, *Similarity and Dimensional Methods in Mechanics*, 10th ed. (CRC Press, Boca Raton, FL, 2018).

[93] R. A. Axford, Laser Part. Beams **18**, 93 (2000).

[94] Z. Boyd, S. Ramsey, and R. Baty, Quarterly J. Mech. Appl. Math. **70**, 401 (2017).

[95] Y. B. Zel'dovich and Y. P. Raizer, *Physics of Shock Waves and High-temperature Hydrodynamic Phenomena* (Courier Corporation, Boston, MA, 2002).

[96] A. L. Velikovich and J. L. Giuliani, Phys. Rev. E **98**, 013105 (2018).

[97] J. C. Slater, *Introduction to Chemical Physics*, International Series in Physics (McGraw-Hill, New York, NY, 1955).

[98] L. D. Landau and K. P. Stanyukovich, On a study of the detonation of condensed explosives, Compt. Rend. (Dokl.) Acad. Sci. URSS **46**, 362 (1945).